

u^b

b
**UNIVERSITÄT
BERN**

Application of Surface Physics for Instruments in Space Science

**Inauguraldissertation der
Philosophisch-naturwissenschaftlichen Fakultät der
Universität Bern**

**vorgelegt von
Martina Föhn**

2021

**Leiter der Arbeit
Prof. Dr. Peter Wurz**

Physikalisches Institut der Universität Bern

Abstract

Contents

1	Introduction	1
2	Theory	3
2.1	Requirements	3
2.2	Basic Theory about TOF Massspectrometry	3
2.2.1	Principle	4
2.2.2	Mass resolution	4
2.2.3	Mass Resolution Error Estimations	5
2.2.4	Signal-to-Noise Ratio and Sensitivity	10
2.2.5	Statistical Peak Analysis	11
2.3	Ion Optical Design, NIM specific elements	11
2.3.1	Filament Power Calculation	11
2.3.2	Ion Storage capability	11
2.3.3	Density enhancement Model	12
2.3.4	Callisto Flyby	19
2.3.5	Shutter Performance	23
2.3.6	Pressure calibration of the NIM Sensor	26
2.3.7	Detector Parameters	26
3	Setup	30
3.1	NIM Sensor Models	30
3.2	Test facilities/ Test Tools	30
3.2.1	Pumpstand nr. 2	31
4	Experiments	39
4.1	Flight Ion-Mirror	39
4.2	Flight Antechamber	40
4.3	Entrance characterization	42
4.4	Shutter Performance Test	46
4.5	Simulations	46
4.6	Filament decision	46
4.7	Pulser	46
4.8	Detector Tests	48
4.9	Ionoptics	50
4.9.1	Voltage Optimisation	50
4.10	Instrument performance tests	51
4.10.1	Prototype	51
4.10.2	PFM	51
4.10.3	FS	51
5	Conclusion	55

6 Outlook	57
References	58
7 Appendix	60

List of Acronyms

BCVD	Boron-doped Chemical Vapour Deposition
DLC	Diamond-Like Carbon surface
EMG	Exponentially Modified Gaussian
ENA	Energetic Neutral Atoms
FWHM	Full Width at Half Maximum
IBEX	Interstellar Boundary EXplorer
ILENA	Imager for Low Energetic Neutral Atoms
IMAP	Interstellar Mapping and Acceleration Probe
JNA	Jovian Neutral Atom Analyser
JUICE	JUpiter ICy moon Explorer
L1	Lagrange 1
LISM	Local InterStellar Medium
MCA	MultiChannel Analyzer
MCP	MultiChannel Plate
PA	PostAcceleration voltage
PEP	Particle Environment Package
RPA	Retarding Potential Analyser

1 Introduction

JUICE PEP NIM

2 Theory

Add a Chapter about electric fields?/ Basis for the simulations?

2.1 Requirements

2.2 Basic Theory about TOF Massspectrometry

Refs./Citations NIM is a time of flight mass spectrometer consisting of, an ion-source, a mass analyser and a detector.

The NIM instrument is able to measure neutrals and ions. Neutral particles get ionised by

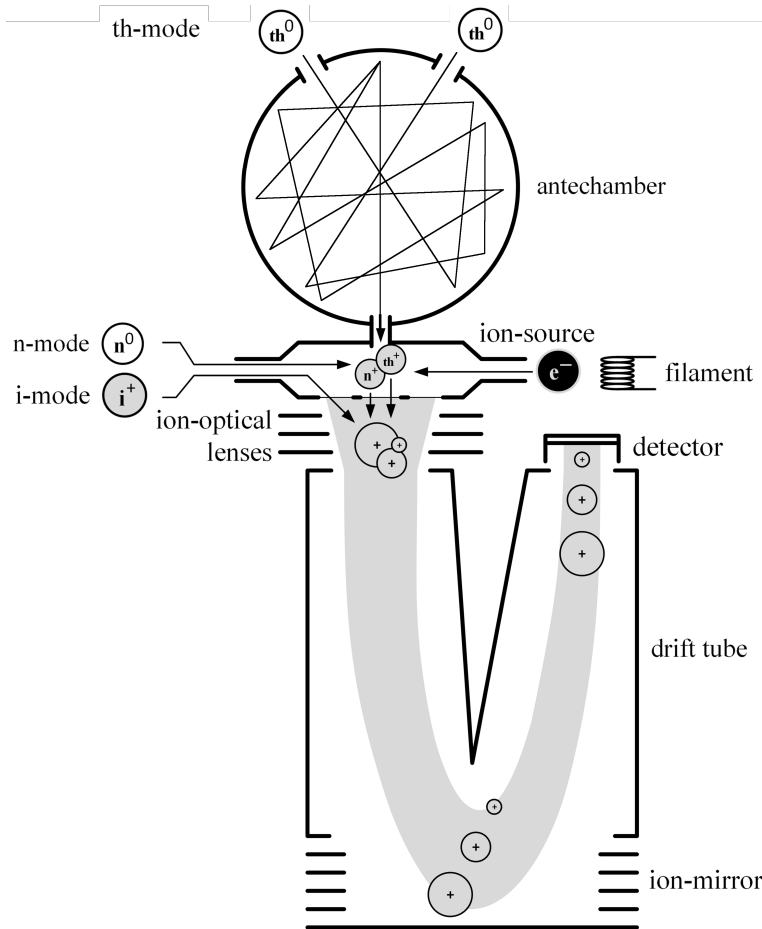


Figure 1: Schematics of the NIM mass spectrometer. Adapted from [10].

electron ionisation. A filament is heated up until it emits electrons. Ions enter the ion source directly. All ions get accelerated to the same energy and fly through the mass analyser. Light particles fly faster through the spectrometer than heavier ones. The different particle species arrive at different times at the detector. To enlarge the flight distance, NIM has an ion-mirror.

2.2.1 Principle

The ions in the ion-source are focused in the centre of the ion-source. When extracting them, a high voltage pulse is applied on the extraction grid to accelerate the ions to the energy W .

$$W = \int_0^{s_0} qE_s ds = \frac{qU_0}{2} \quad (1)$$

With s_0 the distance from the centre of the ion-source to the extraction grid corresponding to half the height of the ion-source. q is the particle charge, E_s is the applied electric field strength induced by the voltage U_0 applied on the extraction grid. The ions start in the centre of the ion-source and not at the backplane. Therefore, they have the kinetic energy $qU_0/2$ when reaching the extraction grid:

$$\frac{qU_0}{2} = \frac{1}{2}mv^2 \quad (2)$$

With m the mass of the particle and v the particle velocity. Rearranging this formula results in:

$$\frac{m}{q} = U_0 \frac{t^2}{D^2} \quad (3)$$

With t the time of flight and D the flight distance from the extraction grid to the detector. In real systems, the energy W and the flight distance D cannot be determined exactly. U_0 and D^2 are merged into one constant C resulting in:

$$\frac{m}{q} = C(t - t_0)^2 \quad (4)$$

t_0 correspond to an offset between the actual start of the mass axis versus the time axis. This offset is induce by the electronics. The two calibration constants C and t_0 are determined by at least knowing two species in the spectrum. With that information, the mass scale is calibrated.

2.2.2 Mass resolution

The mass resolution is calculated as follows. According to Eq.4 m is proportional to t^2 :

$$m = c \cdot t^2 \quad (5)$$

The derivative is:

$$\frac{dm}{dt} = 2 ct \quad (6)$$

$$dm = 2 ct \cdot dt \quad (7)$$

Dividing Eq. (5) through Eq. (7) results in:

$$\frac{m}{dm} = \frac{ct^2}{2 ct \cdot dt} \quad (8)$$

$$\frac{m}{dm} = \frac{t}{2 dt} = \frac{\mu}{2 \cdot FWHM} \quad (9)$$

With μ the centre of the mass peak in the time domain and $FWHM$ is the full width at half maximum of the mass peak.

2.2.3 Mass Resolution Error Estimations

In this chapter, we take a closer look at the different contributions having an impact on the mass resolution of the NIM instrument. The focus is on the contributions originating from the source thus they have the biggest impact on the mass resolution of the instrument.

The total time spread dt_i of the signal of a particle species i is:

$$dt_i = \sqrt{\sum_k dt_k^2} = \sqrt{dt_D^2 + dt_{ADC}^2 + dt_{th}^2 + dt_s^2 + dt_{fall}^2} \quad (10)$$

With the different contributions dt_k . When an ion hits the detector, it generates a voltage pulse with a pulse width dt_D . For the NIM detectors, the pulse width is in the range of ~ 0.5 ns. The generated pulse is converted into a digital signal with an analog-to-digital converter (ADC). The ADC used in the laboratory has a sampling rate of 4 GHz resulting in a time resolution of $dt_{ADC} = 0.25$ ns. The flight ADC has a maximal sampling rate of 2 GHz corresponding to a time resolution of 0.5 ns. The time spreads resulting from the thermal energy of the ions dt_{th} , from the different start positions of the ions within the ionisation region dt_s and from fall time of the high voltage pulse dt_{fall} are coupled because they all affect the energy deviation of the ions. The ions in the ion-source have thermal energy W_{th} :

$$W_{th} = \frac{3}{2} \cdot k_B \cdot T \quad (11)$$

With k_B the Boltzmann constant and T the temperature. The thermal energy leads to an initial velocity of the ions v_{init} (Fig. 2 top panel). In worse case scenario, the velocity vector of one ion points in the direction of the extraction grid (ion 1) and the vector of another ion points in towards the backplane (ion 3). When the extraction pulse is applied on the grid, ion number 1 has to turn around before it is accelerated. When the absolute value of the velocity vector of the two ions is the same, the two ions have the same amount of energy when reaching the extraction grid. Therefore, the time difference dt_{th} between those two ions stays the same. At a certain point in time, these ions will overtake ions with less energy. With the ion-mirror ions with different energies are focused.

The total energy W_{tot} the ions get in the ionisation region when a high voltage pulse is applied on the extraction grid is:

$$W_{tot} = \int_{s_{init}}^{s_0} q \cdot E(t) \cdot ds \quad (12)$$

With s_{init} the initial position of the ions, s_0 the distance from the centre of the ionisation region to the acceleration grid, q the particle charge and $E(t)$ the electric field strength depending on the time t . When the ions start at different positions in the ionisation region s_{init} , they receive a different amount of energy because they travel a different distances in the acceleration field (Fig. 2 lower panel). Ions starting closer at the backplane receive more energy but start later at the extraction grid than ions starting closer to the extraction grid. At a certain point in time, the

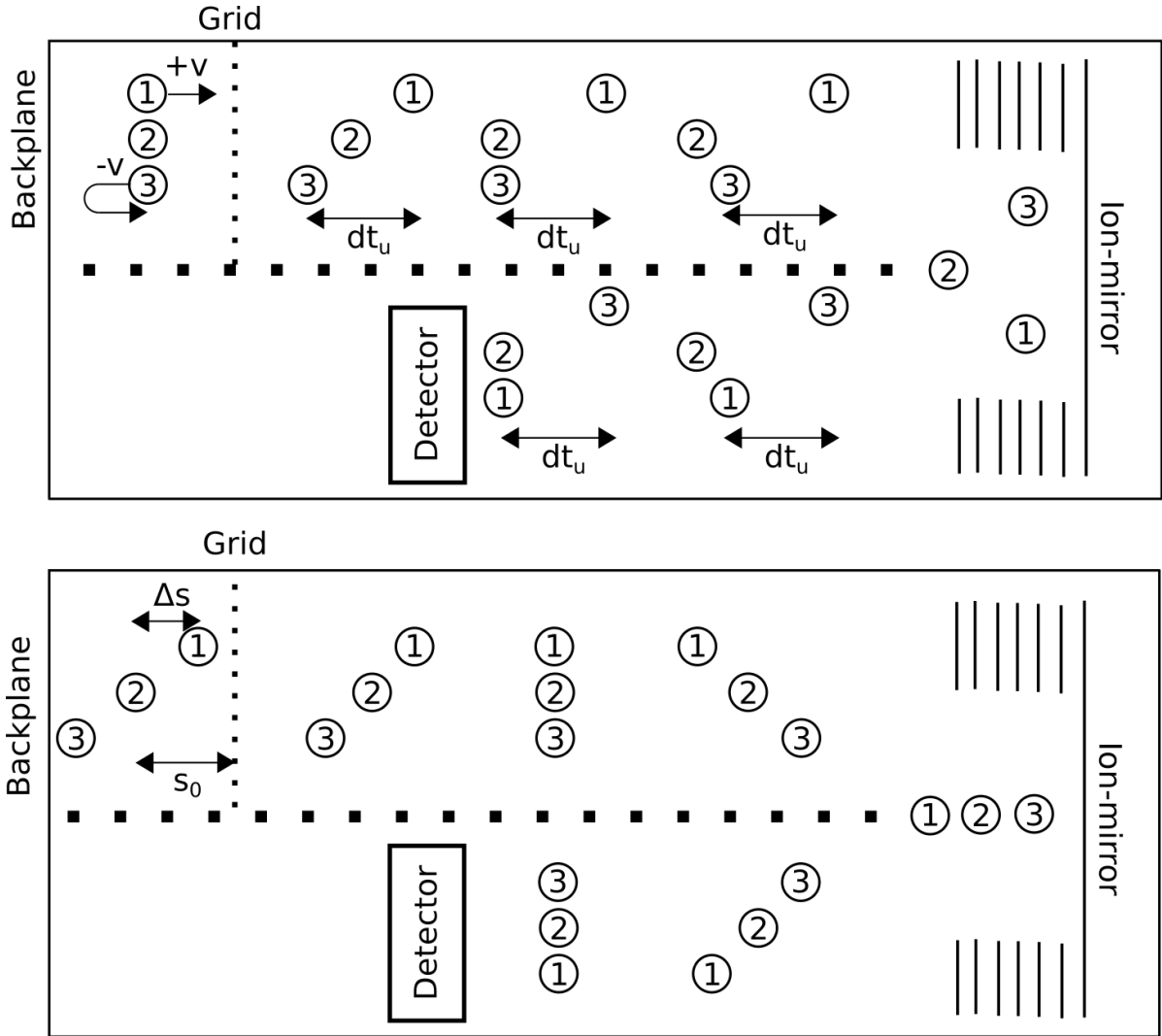


Figure 2: Ion flight path for different start velocities (top panel) and start positions (lower panel).

ions starting closer at the backplane will overtake the other ions. With an ion-mirror ions with different energies are refocused. Ions with higher energy penetrate deeper into the ion-mirror and have a longer flight path. The best position for the detector is when all ions with different energies are at the same position. The time deviation induced by the different start positions of the ions is dt_s .

The ions are accelerated by applying a high voltage pulse on the extraction grid. Fig. 3a) shows the shape of a realistic extraction pulse. The pulser needs the time t_{fall} to charge the extraction grid. Fig. 4 top show the changing electric field as a function of the position for atomar hydrogen (H_1) and oxygen (O_1) in case when these two species start at the same position. The total energy W_{tot} of the ions corresponds to the area under the curves and is plotted on the bottom panel of Fig. 4. Hydrogen is lighter than oxygen and therefore, it leaves the ionisation region earlier. This results in a smaller amount of energy for hydrogen than for oxygen. The

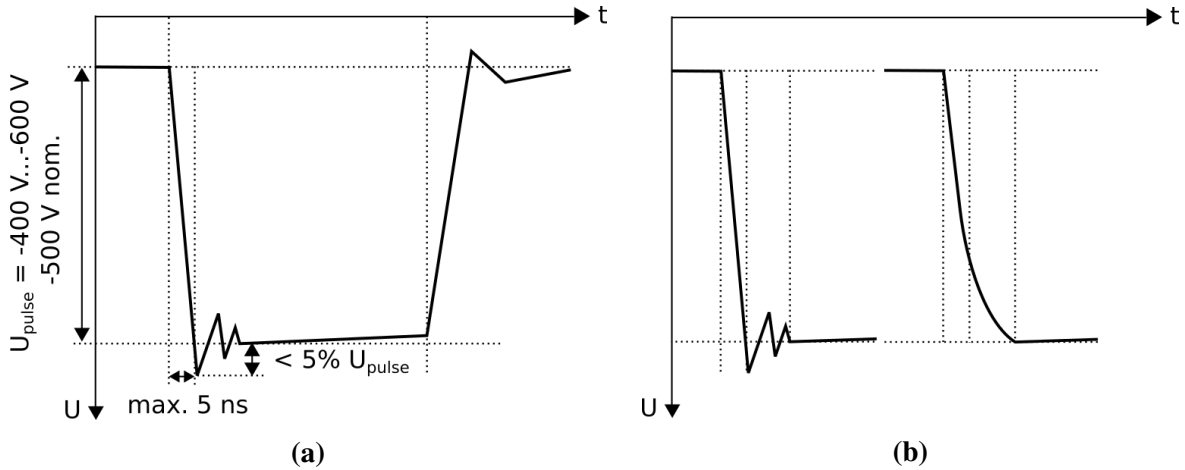


Figure 3: a) Shape of a realistic high voltage pulse applied on the extraction grid. b) Two different possible shapes of the falling edge of the high voltage pulse.

shorter the fall time of the high voltage pulse is, the smaller is the energy difference because it shifts the position of the ions at the fall time $s_i(t_{fall})$ towards zero. When looking at the pulse shape, it is more important to have a small fall time with an overshoot than a pulse slowly converging to the maximum (Fig. 3b) because the resulting energy deviation in the first case is much smaller than in the second.

In the following section the influence of the fall time of the high voltage pulse in combination with the spacial deviation Δs and the thermal energy of the ions on the mass resolution is analysed. To investigate the impact of these effects, this model does not include any focusing lenses and has also no ion-mirror. The detector is positioned 1 m after the extraction grid. The velocity of the ions at the extraction grid is calculated with the equation of motion. The electric field $E(t)$ in the ionisation region is approximated with a linear function during the fall time t_{fall} and it is approximated as a constant during the rest of the time:

$$E(t) = \begin{cases} E_1 \cdot \frac{t}{t_{fall}}, & (0 \leq t \leq t_{fall}) \\ E_1, & t_{fall} < t \end{cases} \quad (13)$$

E_1 is the electric field strength when the high voltage pulse is fully applied:

$$E_1 = \frac{U_0}{2 \cdot s_0} \quad (14)$$

With U_0 the pulse voltage. The equation of motion for the ions during the fall time is:

$$a_{fall}(t \leq t_{fall}) = \frac{q \cdot E_1}{m \cdot t_{fall}} \cdot t \quad (15)$$

With a_{fall} the acceleration of the ions and m the ion mass. The velocity of the ions v_{fall} is:

$$v_{fall}(t \leq t_{fall}) = \frac{q \cdot E_1}{2 \cdot m \cdot t_{fall}} \cdot t^2 + v_{init} \quad (16)$$

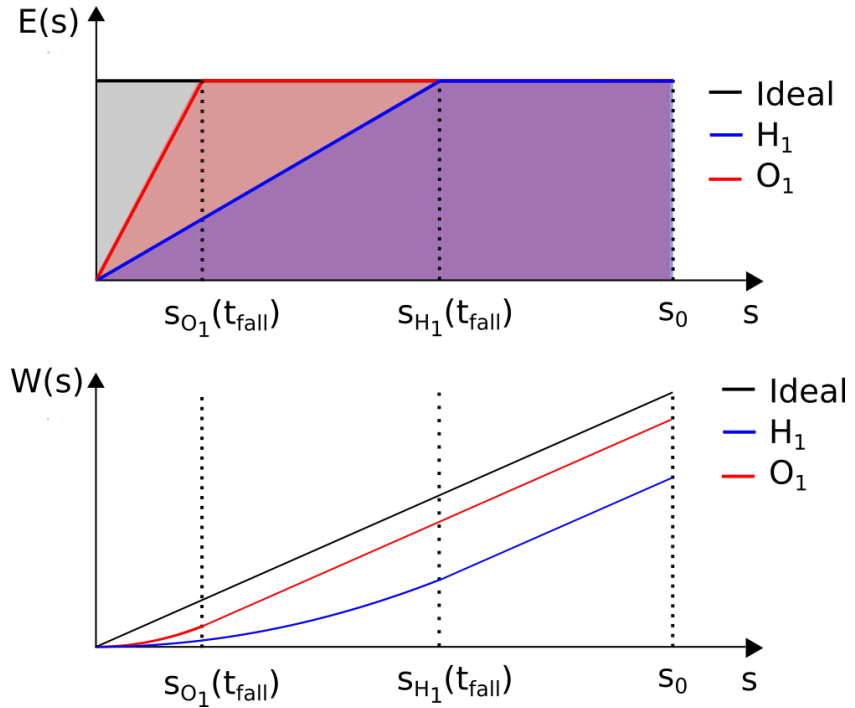


Figure 4: Electric field $E(s)$ an ion experiences, as a function of the distance between the centre of the ionisation region and the extraction grid s_0 for two different species. $s_i(t_{fall})$ is the position of the corresponding species after the fall time t_{fall} .

With v_{init} the initial velocity of the ions before applying the extraction pulse. Integrating over time results in the position of the ions s_{fall} at the time t :

$$s_{fall}(t \leq t_{fall}) = \frac{q \cdot E_1}{6 \cdot m \cdot t_{fall}} \cdot t^3 + v_{init} \cdot t + s_{init} \quad (17)$$

When the high voltage pulse is fully applied and the ions did not reach the extraction grid until that time, the acceleration of the ions a_p is:

$$a_p(t > t_{fall}) = \frac{q \cdot E_1}{m} \quad (18)$$

The velocity v_p is:

$$v_p(t > t_{fall}) = \frac{q \cdot E_1}{m}(t - t_{fall}) + v_{fall}(t_{fall}) \quad (19)$$

With $v_{fall}(t_{fall})$ the velocity of the ions at the time when the pulse reached full high voltage. The position s_p is:

$$s_p(t > t_{fall}) = \frac{q \cdot E_1}{2 \cdot m}(t - t_{fall})^2 + v_{fall}(t_{fall})(t - t_{fall}) + s_{fall}(t_{fall}) \quad (20)$$

With $s_{fall}(t_{fall})$ the position of the ions at the time when the pulse reached full high voltage. When the ions leave the ionisation region before full high voltage is applied on the extraction

grid, the time they spend in the ionisation region t_{IS} is calculated by setting $s_{fall} = s_0$ and solving the cubic Eq. (17) to t . The velocity v_{Grid} of the ions at the extraction grid is determined by inserting t_{IS} in Eq. (16).

When the ions leave the ionisation region after the high voltage is fully applied, the time they spend in the ionisation region t_{IS} is calculated by setting $s_p = s_0$ and solving Eq. (20) to t . The velocity v_{Grid} of the ions at the extraction grid is determined by inserting t_{IS} in Eq. (19). The total flight time of the ions in this model is:

$$t_{TOF} = t_{IS} + \frac{D}{t_D} \quad (21)$$

With D the flight distance from the extraction grid to the detector and the t_D the time the ions need to travel the distance D . The mass resolution is calculated according to Eq. (9). In addition, the deviation of the mass resolution of the ions of the mass/charge ratio i relative to the mass resolution of ions with a mass/charge ratio of 200 is calculated:

$$R = 1 - \frac{m_i/\Delta m_i}{m_{200}/\Delta m_{200}} \quad (22)$$

This deviation is a measure by how many % the mass resolution of the low mass particles deviates from the mass resolution of high mass particles because for high mass particles, the mass resolution reaches a plateau (Fig. 5 left). The mass resolution of mass 200 u was taken as a reference.

The simulations revealed that the impact of the particle temperature is negligible compared to

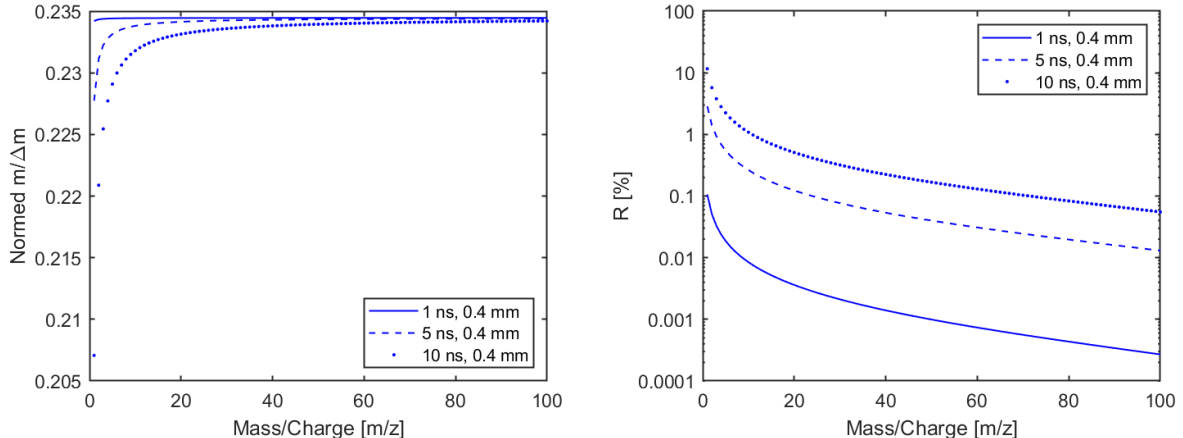


Figure 5: Simulated mass resolution for a linear TOF without any focusing ionoptics as a function of the mass/charge ratio of the particles for three different pulser fall times.

the impact of the position deviation and the pulse fall time. The impact of the fall time is shown in Fig. 5 left. The position deviation is ± 0.4 mm around the start point which corresponds to the diameter of the electron beam in the ionization region of NIM. With decreasing fall time, the deviation in mass resolution decreases. This is also visible in the right figure. An improvement in the fall time by one decade results in an improvement of 1 decade of the

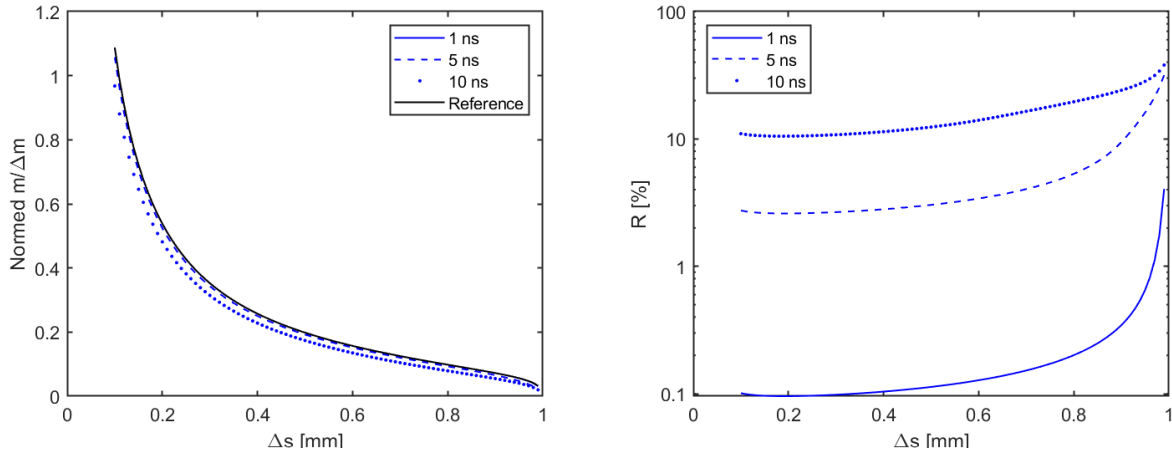


Figure 6: Relative deviation of the mass resolution with reference to the mass resolution of mass 200 u for a linear TOF without any focusing ion-optics as a function of the mass/charge ratio of the particles for three different pulser fall times.

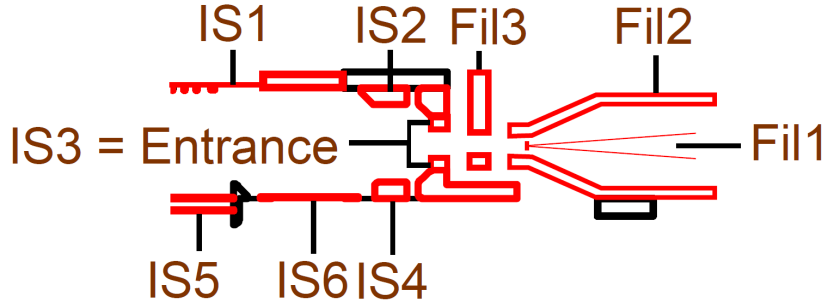


Figure 7: Ionisation region of NIM.

relative error. With a fall time of 1 ns the maximum relative deviation is only 0.1 %. Fig. 6 left shows the mass resolution as a function of the position deviation Δs for mass 1 u. The ionisation region has a diameter of 2 mm. Therefore the maximal deviation of the ions is 1 mm. With increasing Δs the mass resolution drops very rapidly. Therefore it is very important to focus the ions in the centre of the ionisation region. The better the ions are focused, the better is the mass resolution. The focusing electrodes in the ionisation region have to be [Continue here..](#)

2.2.4 Signal-to-Noise Ratio and Sensitivity

SNR

The SNR is defined as the ratio of the background corrected peak amplitude I_P^{max} and the standard deviation of the base line $std(I_b)$ [4], [8]:

$$SNR = \frac{I_P^{max}}{std(I_b)} \quad (23)$$

A high mass resolution improves also the signal-to-noise ratio. By better focusing the ions in the time frame, the peak gets narrower. The area under the peak corresponds to the number of ions. If the number of ions and therefore the area under the curve stays the same, a narrower peak implicates an increase in signal height and therefore in a higher SNR.

Sensitivity

The sensitivity n_{lim} is the actual detection limit of the sensor. It is defined as the amount of gas detected by the instrument n_{det} over the amount of ions entering the instrument n_p times the signal intensity measured by the instrument I_{sig}

$$n_{lim} = \frac{n_p \cdot I_{sig}}{n_{det}} \quad (24)$$

2.2.5 Statistical Peak Analysis

2.3 Ion Optical Design, NIM specific elements

This section gives a detailed overview over the different subcomponents of NIM. Here, the fundamental theory parts for the NIM specific elements are explained. These elements are the functionality of the closed source antechamber, the shutter motor,... Later on in chapter Ref. test results of the different components are shown.

2.3.1 Filament Power Calculation

2.3.2 Ion Storage capability

Ion storage of positive ions is achieved by the negative potential of the electron beam. In the following section, the potential in the centre of the electron beam is calculated. The electron emission current I_{em} is:

$$I_{em} = n_e q_0 v \pi R_e^2 \quad (25)$$

With n_e the electron volume density, q_0 the elementary charge, v the velocity of the electrons and R_e the radius of the electron beam (Fig.8). The electrons get accelerated by the negative potential applied at the filament base. This potential is around -70 V resulting in a kinetic energy U of 70 eV. The velocity of the electrons is:

$$v = \sqrt{\frac{2U}{m_e}} \quad (26)$$

With m_e the mass of the electron. Rearranging Eq. (25) for the volume density n_e and inserting Eq. (26) for the velocity results in:

$$n_e = \frac{I_e}{q_0 \pi R_e^2} \sqrt{\frac{m_e}{2U}} \quad (27)$$

The electric field $E(r)$ in the ionization region is calculated for $R_e < r < h_{Is}/2$ with r the distance from the centre of the beam and h_{Is} the height of the ion source. The electric flux is defined as the surface integral of the electric field through the surface of an enclosed volume which is in this case a cylinder volume. Using Gauss's law the electric flux through the beam surface A_{beam} is equal to the total charge Q inside the cylinder volume.

$$A_{beam}E(r) = \frac{Q}{\epsilon_0} \quad (28)$$

$$2\pi rlE(r) = \pi R_e^2 ln_e q_0 \frac{1}{\epsilon_0} \quad (29)$$

Replacing the number density n_e with Eq. (27) and solving the equation for the electric field E results in:

$$E(r) = \frac{I_e}{2\pi\epsilon_0} \sqrt{\frac{m_e}{2U}} \frac{1}{r} \quad (30)$$

The potential $\Phi(r)$ at a position r inside of the electron beam is:

$$\Phi(r) = - \int_{h_{Is}/2}^r E(r') dr' = - \frac{I_e}{2\pi\epsilon_0} \sqrt{\frac{m_e}{2U}} \ln \left(\frac{R_e}{h_{Is}/2} \right) \quad (31)$$

For calculating the electric field at a point within the electron beam at distance $0 < r < R_e$ we use again Gauss's law:

$$2\pi rlE(r) = \pi r^2 ln_e q_0 \frac{1}{\epsilon_0} \quad (32)$$

Replacing the number density n_e with Eq. (27) and solving the equation for the electric field E results in:

$$E(r) = \frac{I_e}{2\pi\epsilon_0} \sqrt{\frac{m_e}{2U}} \frac{1}{R_e^2} \quad (33)$$

The electric potential $\Phi(r)$ is:

$$\Phi(r) = - \int_{R_e}^r E(r') dr' = - \frac{1}{4\pi\epsilon_0} \sqrt{\frac{m_e}{2U}} \left(\frac{r^2}{R_e^2} - 1 \right) \quad (34)$$

And relative to border of the ion source:

$$\Phi(r) = - \frac{I_e}{4\pi\epsilon_0} \sqrt{\frac{m_e}{2U}} \left(2 \ln \left(\frac{R_e}{h_{Is}/2} \right) + \frac{r^2}{R_e^2} - 1 \right) \quad (35)$$

2.3.3 Density enhancement Model

NIM has an open source entrance where neutral particles and ions enter the ionisation region directly and a closed source entrance where particles enter the ionization region after being thermalized in an antechamber. In this chapter the signal amplification factor of the closed source entrance through the antechamber is determined. The density enhancement model

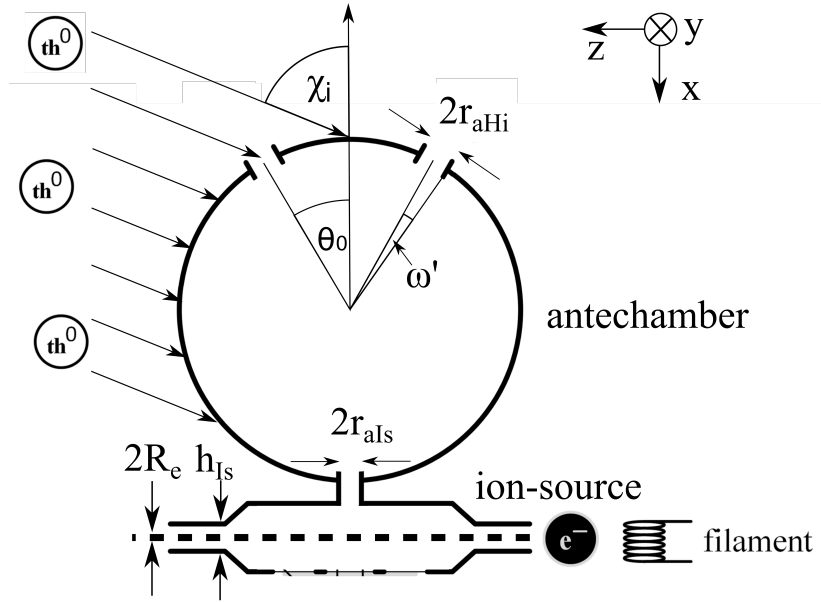


Figure 8: Schematics of the antechamber and the ionisation region.

T_a	295 K	r_{aHi}	2.5 mm	χ	0°
T_s	320 K	r_{aIs}	2 mm	θ_0	30°
k	1	v_{sc}	2.5 km/s	m	18 u
a	0.23				

Table 1: Values used for the variation of the different variables of the antechamber Eq. (36).

described in [14] is used and adapted for the geometry of NIM's antechamber. The particle density n_{cs} in the ionization region is:

$$n_{cs} = n_a \sqrt{\frac{T_a}{T_s}} \cdot \frac{k \cdot \sin^2\left(\frac{\omega}{2}\right) \cdot \cos^2\left(\frac{\omega}{2}\right)}{1 - k \cdot \cos^2\left(\frac{\omega}{2}\right)} \frac{(F(S_1) + F(S_2))}{2} \frac{r_{aIs}^2 \cdot a}{2 \cdot r_{aHi}^2 + r_{aIs}^2 \cdot a} \quad (36)$$

$$F(S_i) = e^{-S_i^2} + \pi^{1/2} \cdot S_i \cdot (1 + \text{erf}(S_i)) \quad (37)$$

With n_a is the particle density of the gas outside the instrument. For the tests in the laboratory n_a is the particle density of then neutral gas beam, in flight it is the particle density of the moons atmosphere. In space T_a is the temperature of the ambient gas and in the laboratory it is the temperature of the neutral particle beam. T_s is the temperature of the antechamber. k is the probability of a particle being re-emitted after colliding with the antechambers inner surface during thermalization and is close to 1 because otherwise the particles would be absorbed.

Ω is the total solid angle summing up all openings through which particles enter the antechamber. NIM has two entrance holes with the same hole diameter and therefore the total

solid angle Ω is the sum of the two solid angles of the entrance holes Ω' :

$$\Omega = 2 \cdot \Omega' \quad (38)$$

All openings into the antechamber have a circular shape therefore, the solid angle Ω is replaced by an angle ω in the x-z-plane to simplify the equation [5].

$$2\pi(1 - \cos(\omega)) = 2 \cdot 2\pi(1 - \cos(\omega')) \quad (39)$$

$$\cos(\omega) = 2\cos(\omega') - 1 \quad (40)$$

$$\omega = \cos^{-1}(2\cos(\omega') - 1) \quad (41)$$

ω' is the half angle of one entrance hole (Fig. 8).

S_i in Eq. (37) is the speed ratio along the normal axis of the entrance hole:

$$S_i = \begin{cases} 0, & \cos(\chi \pm \theta_0) < 0 \\ v_{sc} \cdot \cos(\chi + \theta_0) \cdot \sqrt{\frac{m}{2k_B T_a}}, & i = 1 \\ v_{sc} \cdot \cos(\chi - \theta_0) \cdot \sqrt{\frac{m}{2k_B T_a}}, & i = 2 \end{cases} \quad (42)$$

with v_{sc} the velocity of the neutral gas beam relative to the antechamber corresponding to the spacecraft velocity, m the average particle mass of the gas and k_B the Boltzmann constant. χ is the angle of the test gas relative to the x-axis of the instrument and θ_0 is the angle between the x-axis and the axis normal of the entrance hole. $\chi \pm \theta_0$ is the angle between the normal axis of the entrance hole and the gas influx direction. $\chi \pm \theta_0$ has to be between $\pm 90^\circ$ to enter the antechamber which implies that $\cos(\chi \pm \theta_0)$ cannot have negative values. $i = 1$ is the index of one of the two entrance hole and $i = 2$ is the index of the other entrance hole.

The antechamber has three openings for the gas to flow out of the antechamber. The last term in Eq. (36) gives the ratio of how many particle leave the antechamber through the hole connecting the antechamber with the ionization region compared to the amount of particles leaving the antechamber through the two entrance holes. The radius of the entrance holes is r_{aHi} and the radius of the hole connecting the antechamber with the ionization region is r_{aIs} . This term takes the molecular flow conductance of the different holes into account. The molecular flow conductance of a thermalized gas is C_0 :

$$C_0 = A\bar{v}/4 \quad (43)$$

with A the cross-section of the opening and \bar{v} the average velocity of the thermalized gas flowing through that opening. This formula is only valid in case the length of the tube is close to zero. Otherwise, the transmission probability a has to be added resulting in:

$$C = C_0 \cdot a \quad (44)$$

The transmission probability depends on the length-to-radius ratio L/R of the opening. D. van Essen and W. Chr. Heerens compared different approaches to determine the transmission probability and give values for specific length-to-radius ratios [13]. The approximation

which comes closest to reality is the one by Nawyn and Meyer. To calculate the transmission probability for any length-to-radius ratio, this data was fitted with the following function:

$$a = y_0 + A_1 \left(1 - e^{-\frac{L/R}{t_1}} \right) + A_2 \left(1 - e^{-\frac{L/R}{t_2}} \right) \quad (45)$$

The fit parameters are listed in Table 2. For the two gas entrance openings of the antechamber

A_1	-0.48 ± 0.01	t_1	7.4 ± 0.3
A_2	-0.45 ± 0.01	t_2	1.13 ± 0.04
y_0	0.998 ± 0.001		

Table 2: Fit parameters of Eq. (45).

a is 1 because they have a sharp edge and therefore the length of the opening is close to zero. The opening between the antechamber and the entrance has a length-to-diameter ratio of 8 resulting in a a of 0.23. The amount of gas flowing through this opening relative to the total outflow is:

$$G_{open} = \frac{C_{aIs}}{C_{aIs} + 2 \cdot C_{aHi}} \quad (46)$$

$$G_{open} = \frac{\frac{r_{aIs}^2 \cdot a \cdot \bar{v}}{4}}{\frac{r_{aIs}^2 \cdot a \cdot \bar{v}}{4} + 2 \frac{r_{aHi}^2 \cdot \bar{v}}{4}} \quad (47)$$

$$G_{open} = \frac{r_{aIs}^2 \cdot a}{r_{aIs}^2 \cdot a + 2 \cdot r_{aHi}^2} \quad (48)$$

With $r_{aIs} = 2$ mm and $r_{aHi} = 2.5$ mm resulting in $G_{open} = 0.067$ meaning that about 6.7% of all particles entering the antechamber actually reach the ionization region due to losses of the geometry.

In the following section the different parameters of the density enhancement equation Eq. (36) were varied to determine their influence. For this analysis the particle density in the ionization region n_{cs} was divided by the particle density of the test gas n_a outside of the antechamber and n_a was set 1 to get the amplification factor of the antechamber. For this analysis the parameters were set according to Table 1 unless otherwise mentioned. The temperatures are the ones used in the laboratory. The used particle velocity was 2.5 km/sec because it is velocity of the spacecraft in Ganymede orbit and the velocity at which most of the measurements will be done.

The first parameter which was varied was the gas temperature T_a . This temperature can be varied between 0 and 1000 K without significantly influencing the gain of the antechamber as it can be seen in Fig. 9. When looking closer, a slight increase in gain is observed with

increasing temperature.

The temperature of the antechamber T_s has a bigger impact on the gain. Ideally this temperature should be as low as possible to slow down the particles when they hit the chamber walls. When the temperature of the antechamber is too low, the gas condenses at the antechamber walls. Therefore the antechamber is kept at temperatures higher than -17 °C during measurements to avoid condensation.

Rewrite captions. The next parameter is the radius r_{aIs} of the hole connecting the antechamber

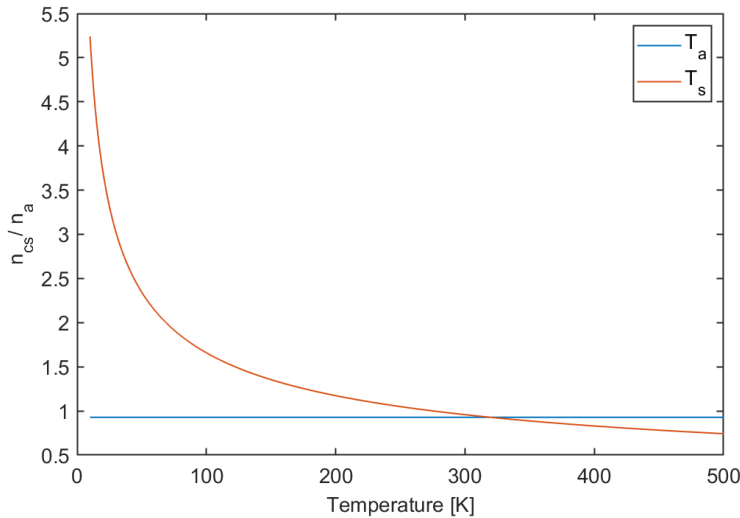


Figure 9: Gain n_{cs}/n_a of the antechamber one time varying the ambient gas temperature T_a and one time varying the antechamber wall temperature T_s according to Eq.(36).

with the ionisation region. When the hole gets bigger, also the amount of gas flowing into the ionisation region increases as it can be seen in Fig. 10. The radius of the entrance holes r_{aHi} should be small to reach a high gain. This has two reasons: When the entrance holes are big compared to the hole connecting the antechamber with the ionisation region, a big amount of gas flows out through the entrance holes. The size of the entrance holes has also an impact on the opening angle ω . In the first designs of such antechambers, the ionisation and counting of the particles happened in the antechamber itself [5]. Therefore the antechamber needed only one opening. Our instrument has two entrances for particles. One to measure them directly without any interaction with the instrument surface (open-source channel) and a closed-source entrance through the antechamber to amplify the signal. Due to the flyby trajectories of the space craft the antechamber has to have entrance holes with angle $\theta_0 = 30^\circ$ relative to the x-axis of the instrument. **Rewrite** When having only one big entrance hole, the gas gets easily reflected and leaves the antechamber before being counted in the antechamber. Therefore a small opening is favoured over a big opening. From that perspective, the biggest gain is achieved when the radius of the entrance hole is 0 ergo the entrance hole is closed. That's the limitation of Eq. (36) is. It does not take into account that at a certain radius of the opening, the gain should decrease because not enough particles enter the chamber to get amplified.

It is very important to take materials with a high particle reflection coefficient k for the coating

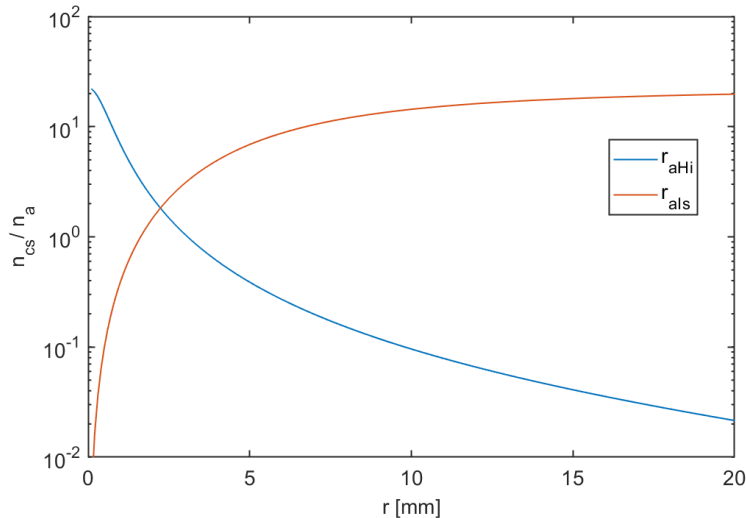


Figure 10: Gain n_{cs}/n_a of the antechamber as a function of the entrance hole radius r_{aHi} and the radius connecting the antechamber with the ionisation region r_{als} .

of the antechamber' s inner surface. The particle reflection coefficient gives the probability of a particle being re-emitted when hitting the surface thus this value has to be close to 1. For our antechamber we used gold because it is electrically conductive preventing the surface from charging in the strong radiation field of Jupiter and it is chemically inert and thus there is a low probability of building chemical bonds with the test gas. Fig. 11 shows the amplification of the antechamber in dependence of k . When changing k by 1% this already has a huge impact on the amplification. The impact of k also depends on ω . A small ω implies a big surface area with which the particles can interact before leaving the antechamber. The more interactions with the antechamber surface are possible, the bigger is the influence of k . For our antechamber ω is about 5.06 ° which is very small and therefore a small change in k has a big impact on the gain.

Fig 12 shows the amplification of the antechamber in dependence of the particles unit mass [u]. The figure shows that particles with higher unit mass get amplified more and are therefore easier to detect.

Fig. 13 shows the amplification of the antechamber in dependence of the spacecraft velocity for different species. We expect H₂O and different radiolysis products such as H₂, O₂ or HO. Absorption lines in the near infrared recorded by the Near Infrared Mapping Spectrometer (NIMS) on board of the Galileo spacecraft indicate CO₂ bond to other solid materials in the soil. Sulphur is part of the plasma. The sulphur compounds are therefore a result of the ion bombardment on the moons surface. Sulphur reacts with water resulting in various different compounds such as sulphur dioxide (SO₂) or sulphuric acid (H₂SO₄) [2]. **include Audrey's paper if it gets finished in time.** Fig. 13 shows that with increasing flyby velocity, the particles get more amplified. Species with higher masses are stronger amplified than light particles as it was already shown also in Fig. 12.

Fig. 14 shows the amplification in dependence of different particle influx angles χ . χ is

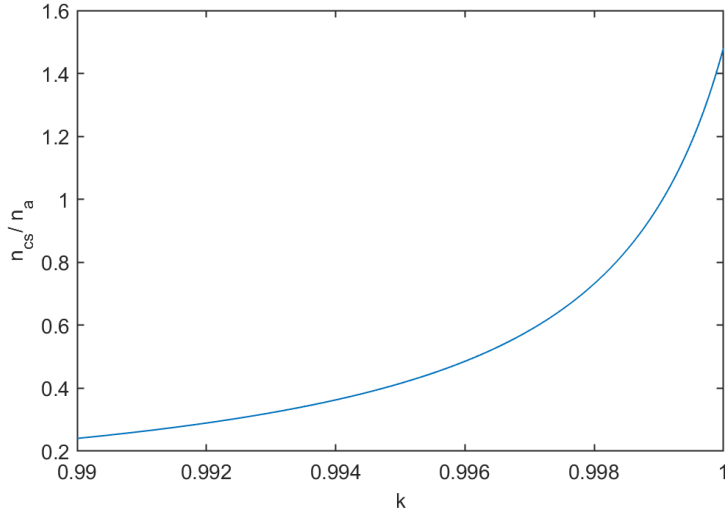


Figure 11: Gain n_{cs}/n_a of the antechamber as a function of the particle reflection coefficient k .

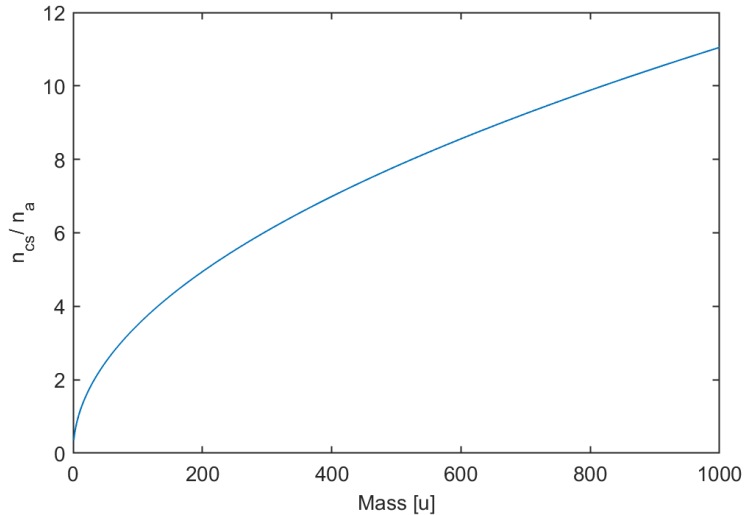


Figure 12: Gain n_{cs}/n_a of the antechamber as a function of the particle mass m .

measured in the x-/y- plane (Fig. 8). The function was evaluated for different positions of the entrance holes. The minimal angle the two entrance hole can be apart from each other without overlapping is 3.6° . The holes of the PFM are at $\theta_0 = \pm 30^\circ$. With that configuration the biggest signal intensity is measured with a spacecraft ramp direction of 0° . When the two holes are at $\pm 60^\circ$ it results in a plateau between $\pm 60^\circ$ and also a wider angular range at which NIM is sensitive. This is an interesting feature under certain circumstance. For our purpose it is unnecessary because the spacecraft blocs the field of view (FoV) for angles bigger than 100° (see also Chap. 2.3.4).

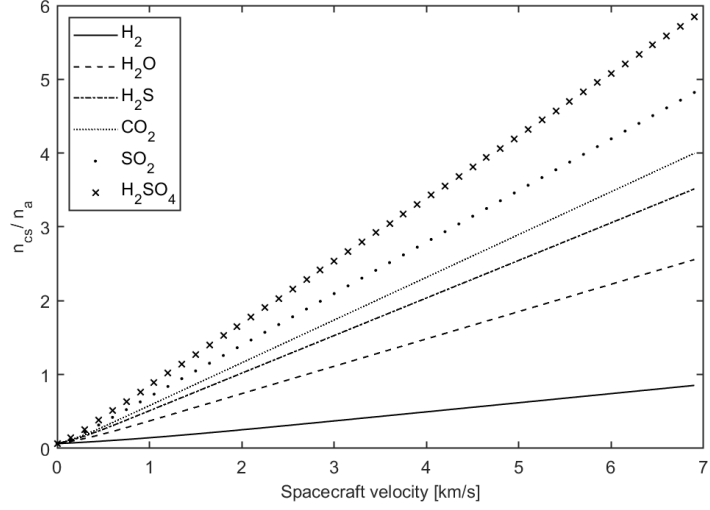


Figure 13: Gain n_{cs}/n_a of the antechamber as a function of the spacecraft velocity v_{sc} for different species expected in the moons atmospheres.

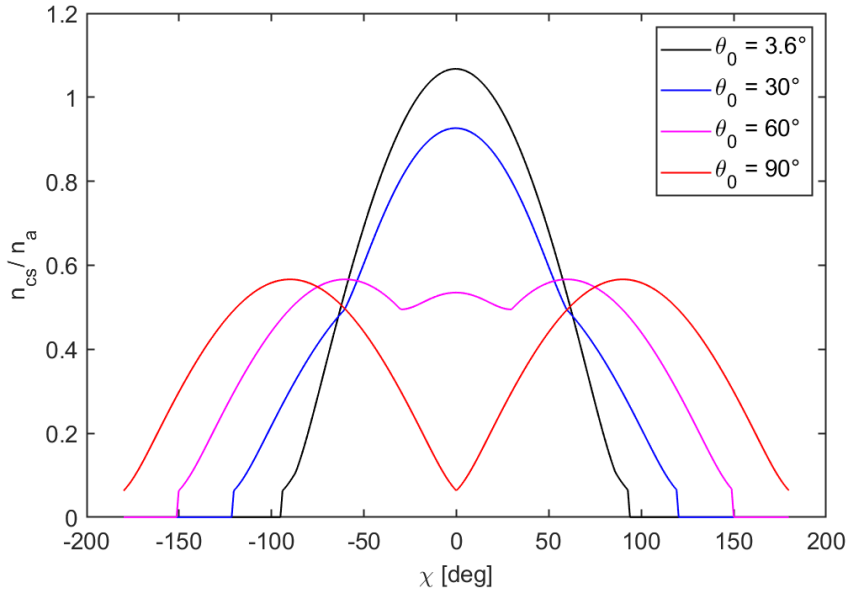


Figure 14: Gain n_{cs}/n_a of the antechamber as a function of the gas influx direction χ for different positions of the two entrance holes θ_0 . $\theta_0 = 30^\circ$ is the position of the holes in flight configuration.

2.3.4 Callisto Flyby

Fig. 16 - Fig. 21 show the changing FoV of the NIM instrument at different times during the fourth Callisto flyby of trajectory 141a [1]. The reference coordinate system for these graphics is the ecliptic coordinate system. During the flyby, the spacecraft changes its orientation in ref-

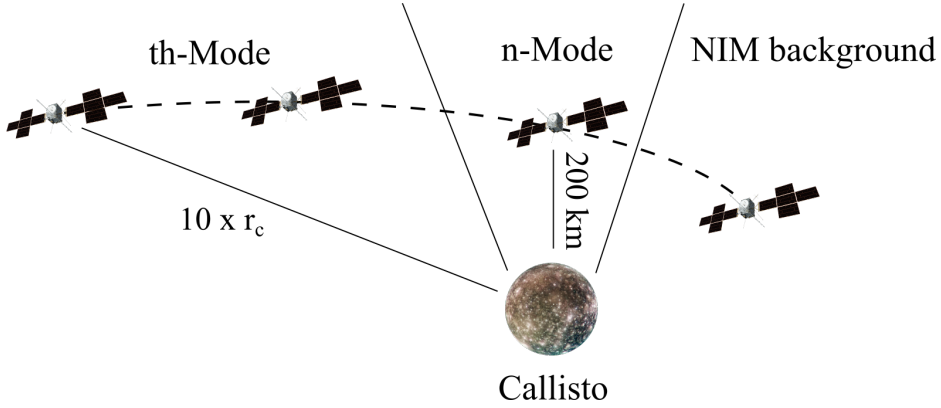


Figure 15: Schematics of one of the flybys at Jupiter’s moon Callisto.

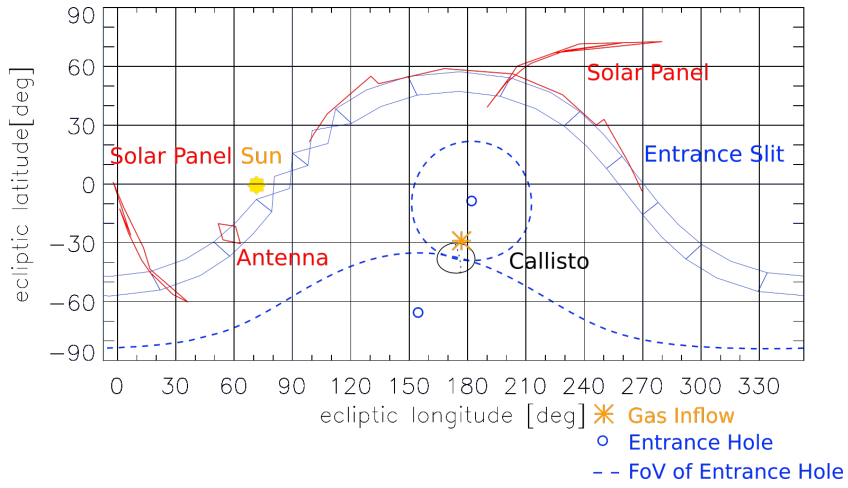


Figure 16: Fourth Callisto flyby of trajectory 141a [1] 1 h before closest approach 15'600 km away from Callisto.

erence to that coordinate system leading to a distortion of the different objects in the figures. The entrance holes of the antechamber are blue circles, the FoVs of the entrance holes are marked as dashed blue lines, the entrance slit is the blue band with the sinusoidal shape. The solar panels and the antenna which bloc part of the FoV of NIM are marked in red. The gas inflow direction is marked as an orange star. Fig. 16 shows the FoV 1 h before closest approach 15'600 km above Callisto’s surface. The gas inflow direction is in between the two entrance holes. The black dotted line on the moon’s surface marks the day/night separation line. As the spacecraft moves closer to the moon, the gas inflow direction moves towards the entrance slit. 5 min before closest approach, NIM changes from thermal to neutral mode (Fig. 18) to be ready for the neutral mode measurements. At this time, the gas inflow direction is still in the FoV of the antechamber. The time window for measuring with the neutral gas mode is very narrow. Already 5 min after closest approach, the gas inflow direction is below the FoV of the neutral gas channel (Fig. 21). Therefore, the time to switch from thermal to neutral mode has to be very short to minimize the number of lost measurements. These measurements are

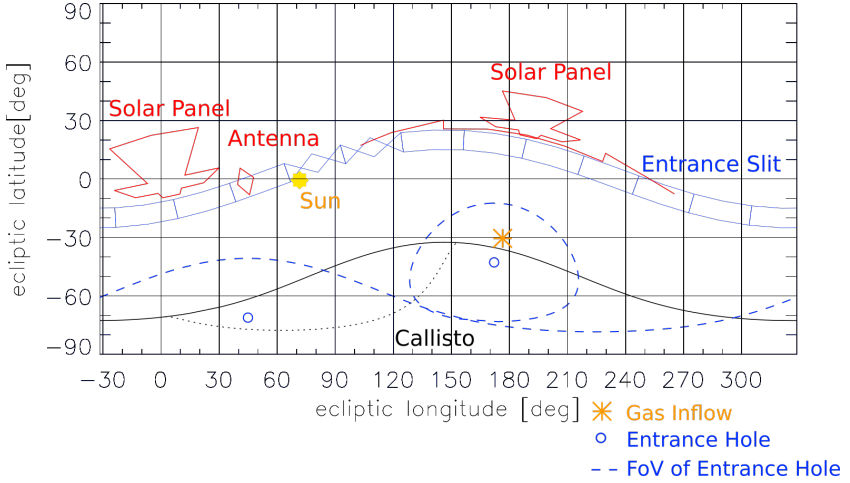


Figure 17: Fourth Callisto flyby of trajectory 141a [1] 10 min before closest approach 1'560 km away from Callisto.

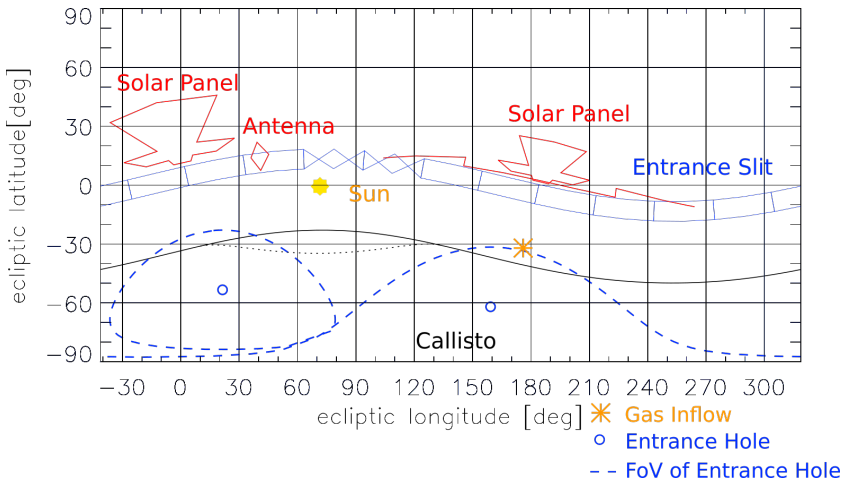


Figure 18: Fourth Callisto flyby of trajectory 141a [1] 5 min before closest approach 580 km away from Callisto.

very crucial because the closer the spacecraft gets to the moon's surface, the higher is the exospheric pressure and therefore the signal intensity.

The spacecraft structure blocs angles higher than 100° . The gas striking the spacecraft sputters particles from the spacecraft's surface. NIM is not able to determine if these particles are part of the moons exosphere or if they originate from the spacecraft. When the gas inflow direction reaches angles higher than 100° NIM starts measuring background. The solar panels are adjusted perpendicular to the sun to maximize power generation. 10 min before closest approach, the solar panels are tilted to leave open the FoV of NIM to measure with the neutral gas mode. In case the solar panels would stay perpendicular to the sun, the gas would graze the surface of the solar panel as it is shown in Fig. 19. Fig. 20 shows the same scenario but with the solar panels tilted to leave open NIM's FoV of the neutral gas channel.

Fig. 22 shows the gain of the antechamber with the total FoV of the two entrance holes marked

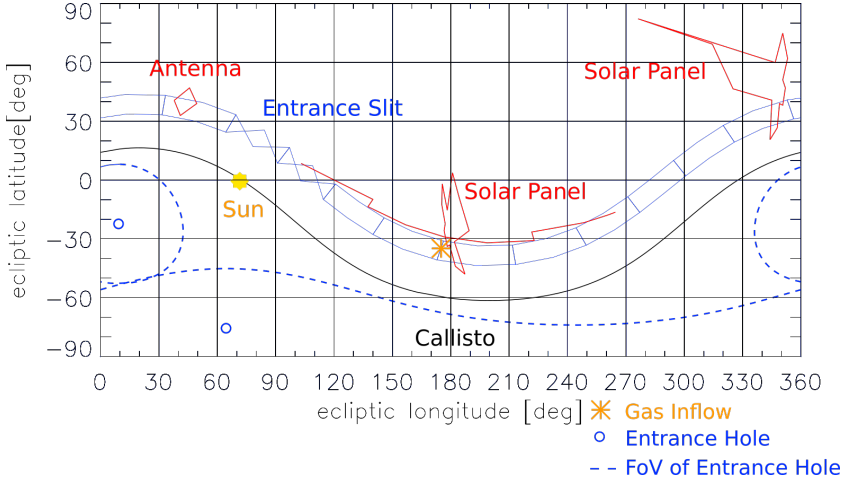


Figure 19: Fourth Callisto flyby of trajectory 141a [1] closest approach 200 km away from Callisto with the solar panels oriented toward the sun to maximizes power generation of the spacecraft.

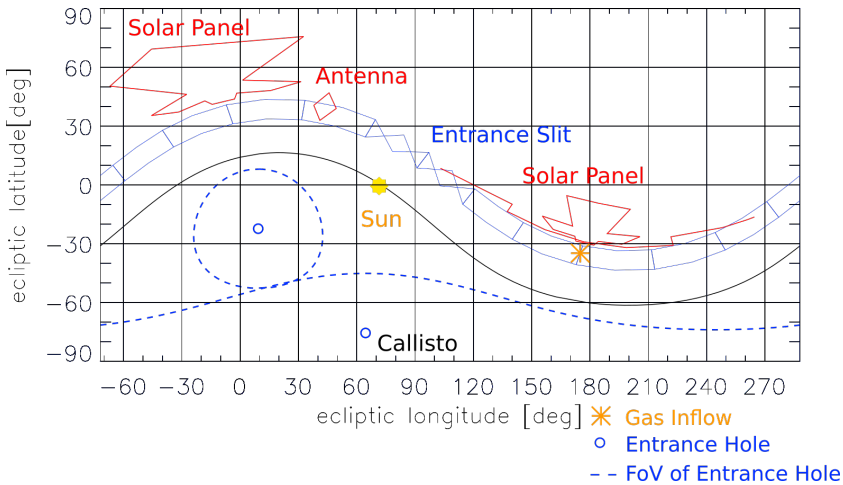


Figure 20: Fourth Callisto flyby of trajectory 141a [1] closest approach 200 km away from Callisto.

as red area $\pm 30^\circ$ around the position of the two entrance holes. The orange stars mark the gas inflow direction for the various scenarios mentioned before. The main gas inflow direction varies for the different flybys. One time the gas comes from positive and one time from negative χ direction. Therefore, it was decided to make two entrance holes to allow measurements with angles different to the main direction to enlarge the FoV of the antechamber. The holes should also not be too close at the entrance because structures of the spacecraft bloc angles bigger than 100° and an amplification of such big angles would be useless.

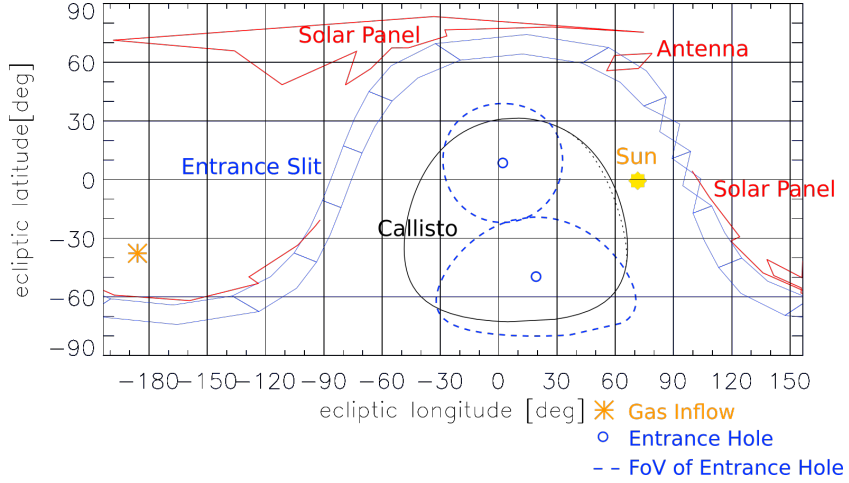


Figure 21: Fourth Callisto flyby of trajectory 141a [1] 5 min after closest approach 640 km away from Callisto.

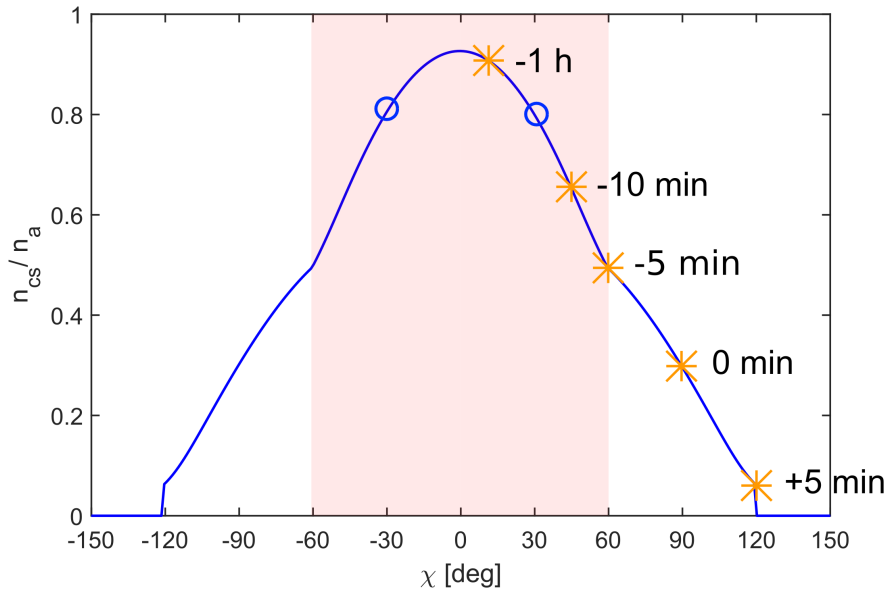


Figure 22: Gain n_{cs}/n_a of the antechamber in dependence of the gas influx direction χ . The blue circles mark the entrance hole positions and the red area marks the FoV of the entrance holes. The stars mark the gas influx direction from 1 h before until 5 min after closest approach of trajectory 141a [1].

2.3.5 Shutter Performance

NIM has a shutter to close the entrance to the antechamber. This shutter is mounted between the ion source and the antechamber (Fig. 23 left). When the shutter is open, the gas flows right through the hole into the ion source. When the shutter is closed, the hole moves to the side as it is indicated in Fig. 23 right. Because the shutter does not close the gag perfectly, still a small

amount of gas flows around the shutter into the ionisation region. In the following section, the geometry factor G_{close} of the antechamber is determined when the shutter is closed.

The molecular flow conductance is:

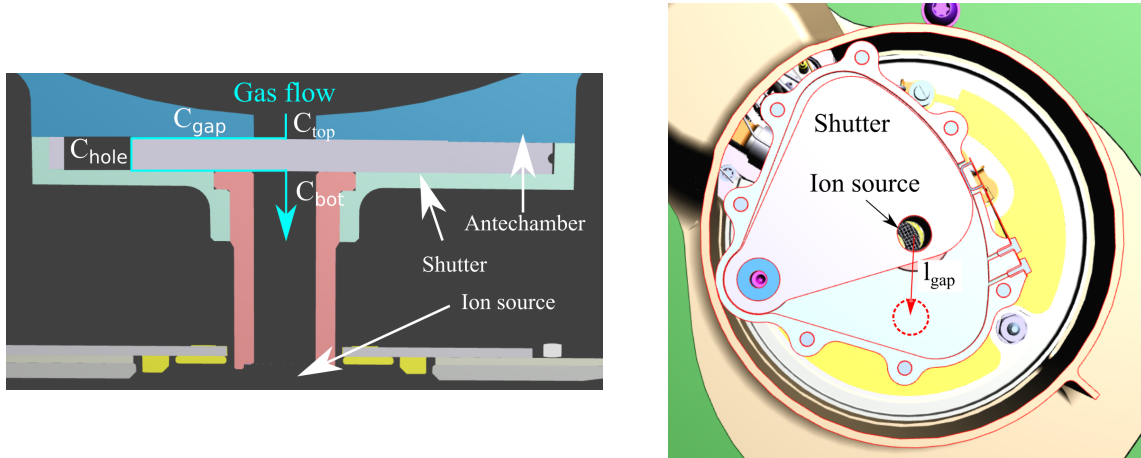


Figure 23: Shutter Motor. Left: side view with shutter closed. Right: Top view with open shutter. When the shutter is closing the central hole moves to the red position.

$$C = \frac{A \cdot \bar{v} \cdot a}{4} \quad (49)$$

With A the cross-section of the tube, \bar{v} the average velocity of the thermalized gas flowing through the opening and a the transmission probability depending on the length-to-diameter ratio of the tube. When the shutter is closed, the conductance of the tube C_{tot} is divided into four terms: The conductance of the upper part of the tube C_{top} , the conductance of the gap between the shutter and pocket C_{gap} , the conductance of the hole in the shutter C_{hole} and the conductance of the lower part of the tube connecting the antechamber with the ionization region C_{bot} (Fig.23 left):

$$C_{top} = \frac{r_{aIs}^2 \cdot \pi \cdot \bar{v} \cdot a_{top}}{4} \quad (50)$$

$$C_{gap} = \frac{2 \cdot r_{aIs} \cdot \pi \cdot h_{gap} \cdot \bar{v} \cdot a_{gap}}{4} \quad (51)$$

$$C_{hole} = \frac{r_{aIs}^2 \cdot \pi \cdot \bar{v} \cdot a_{hole}}{4} \quad (52)$$

$$C_{bot} = \frac{r_{aIs}^2 \cdot \pi \cdot \bar{v} \cdot a_{bot}}{4} \quad (53)$$

With a_i the transmission probabilities of the different sections (Eq. (45)), h_i the height of the different sections, r_{aIs} the radius of the antechamber hole and l_{gap} the minimal distance between the hole in the shutter and the tube connecting the antechamber with the ion-source. The nominal values for these parameters are listed in Table 3. The average velocity \bar{v} will cancel out later in the derivation of the geometry factor. The conductance of the tube C_{tot} is:

$$\frac{1}{C_{tot}} = \frac{1}{C_{top}} + \frac{2}{C_{gap}} + \frac{1}{C_{hole}} + \frac{1}{C_{bot}} \quad (54)$$

a_{top}	0.73	h_{top}	1.5 mm
a_{gap}	0.07	h_{gap}	0.01 mm
a_{hole}	0.67	h_{hole}	2 mm
a_{bot}	0.28	h_{bot}	12 mm
r_{aIs}	2 mm	l_{gap}	7 mm

Table 3: Nominal transmission probabilities a_i , tube heights h_i , tube radius r_{aIs} and minimal gap length l_{gap} when the shutter between the antechamber and the ion-source is closed.

The conductance of one of the entrance holes of the antechamber is:

$$C_{aHi} = \frac{r_{aHi}^2 \cdot \pi \cdot \bar{v}}{4} \quad (55)$$

The geometry factor of the tube when the shutter is closed G_{close} is:

$$G_{close} = \frac{C_{tot}}{C_{tot} + 2 \cdot C_{aHi}} \quad (56)$$

The gap between the shutter and the antechamber has to be very thin to seal the hole when

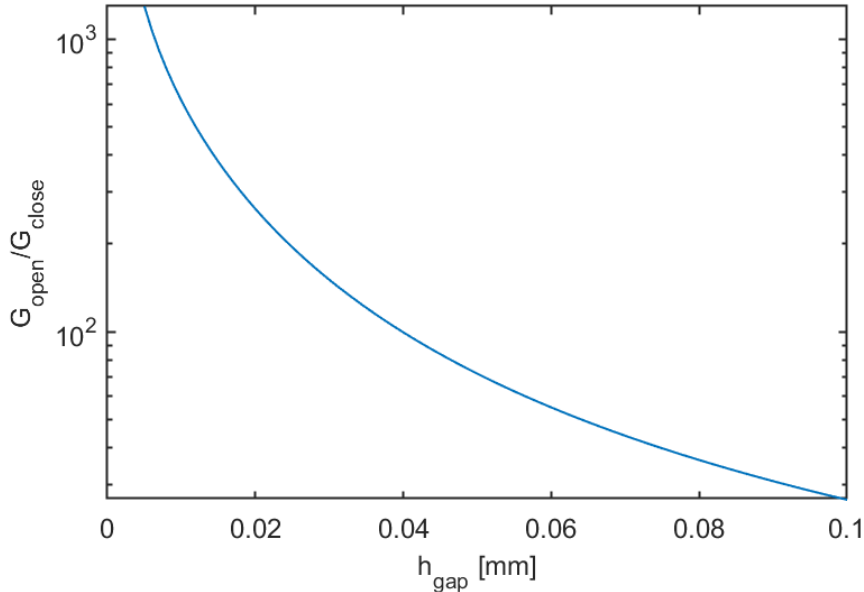


Figure 24: Damping factor G_{open}/G_{close} of the shutter as a function of the gap size h_{gap} of the gap between the shutter and antechamber.

the shutter is closed. Fig. 24 shows the damping factor G_{open}/G_{close} as a function of the gap

size h_{gap} . With increasing gap size, the damping factor reduces significantly. The requirement was to damp the signal by a factor 1000 when the shutter is closed. With the nominal gap size of 0.01 mm, the shutter damps the signal by a factor 600. When the gap size is about 0.1 mm the damping factor is only about 25. This may happen when the shutter is not properly fabricated and the tolerances are therefore bigger than originally designed.

When measuring with the open source channel, a small amount of gas will enter the ion-source through the antechamber. The open source slit is in the y-z-plane and therefore χ is 90° (Fig.8). When the shutter is closed, about 0.05% of the signal originates from the antechamber.

2.3.6 Pressure calibration of the NIM Sensor

see also density enhancement book for that derivation!!! To calculate the number of ions produced in the ion source we use:

$$I_{ion} = \beta \cdot Q_{ion} \cdot L \cdot n \cdot I_{em} \quad (57)$$

With β the extraction efficiency which is 1, L as the effective ionising path in our case 4 mm, n the particle density, I_{em} the electron emission current from the filament and Q_{ion} the ionising cross section. The cross sections of species used in our calibration can be found in table

Write something about the radiation shielding concept? Or just make a reference to the paper because it gives an overview over the concept as far as it is necessary.

2.3.7 Detector Parameters

In this section we calculated some important parameters of the detector such as the dead time and the gain.

Dead time

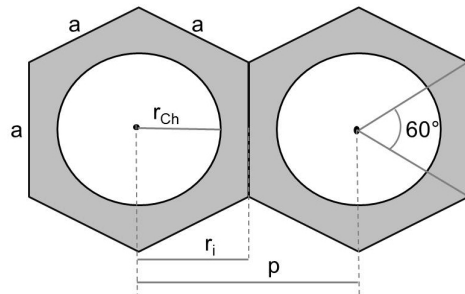


Figure 25: MCP honeycomb structure [9].

The number of channels N of an MCP is its active area A_{act} divided by the area of one channel A_{hex} . The MCP has a honeycomb like structure (Fig. 25). Thus, the area of one channel is the

area of a hexagon:

$$N = \frac{A_{act}}{A_{hex}} = \frac{2 \cdot \pi r_{act}^2}{\sqrt{3} p^2} \quad (58)$$

r_{act} is the radius of the active area of the MCP which is for our MCPs 8 mm and p is the distance between the centres of two channels which is 6 μm . This results in $1.6 \cdot 10^6$ channels. The resistance of a single channel is the resistance of the whole MCP plate R_{MCP} times the number of channels N :

$$R_{ch} = R_{MCP} \cdot N \quad (59)$$

Its resistance depends on the voltage applied over the plate. For a nominal voltage of 1000 V R_{MCP} is $\sim 70 \text{ M}\Omega$ resulting in channel resistance of about $10^{14} \Omega$.

The MCPs consist of two different materials: the structure (grey) consists of a type of lead glass and the hole, which can be approximated with vacuum (white) (Fig.25). The area of the structure is equal to the area of the hexagon A_{ch}^{hex} minus the area of the channel hole A_{ch}^{hole} . the capacitance of one channel C_{ch} is:

$$C_{ch} = \frac{\epsilon_0(\epsilon_r \cdot (A_{ch}^{hex} - A_{ch}^{hole}) + A_{ch}^{hole})}{l_{ch}} \quad (60)$$

With ϵ_0 the vacuum permittivity, ϵ_r the relative permittivity of lead glass and l_{ch} the MCP thickness which is 0.3 mm. The relative electric permittivity depends strong on the conditions under which the material is used for example under which voltage, frequency or temperature the MCPs are used. Furthermore, the manufacturer does not give details about the material characteristics as it is a company secret. In [9] is an analysis of different values for ϵ_r found in literature. These values are between 6 and 20. With these values, the resulting capacity is 5 aF per channel. The dead time of a single MCP channel is the channel resistance R_{ch} times the channel capacitance C_{ch} :

$$\tau = R_{ch} \cdot C_{ch} \quad (61)$$

This results in a dead time of 500 μs . A typical waveform has a duration of about 100 μs . When an ion hits a channel, this channel would be blind for the next five waveforms. With $1.6 \cdot 10^6$ channels and assuming a uniform distribution of particles on the MCP surface, saturation is assumed at particle rates higher than 10^9 particles/s.

$$U(t) = U_0 \cdot (1 - e^{-t/\tau}) \quad (62)$$

It is the time needed to recharge a single channel to approximately 63% of its original charge. After 5τ 99% of the original charge is replenished.

Gain

The following derivation is strongly based on the lecture notes of [15]. When an incoming particle hits the MCP channel wall there is a certain chance that it ejects an electron out of the channel wall. By applying an electric field E over the MCP plate, this electron gets accelerated until it hits the opposite wall, where it ejects more electrons:

$$E = \frac{U_{MCP}}{l} = \frac{F}{q_0} = \frac{am_e}{q_0} \quad (63)$$

With U_{MCP} the voltage applied over the MCP, l the channel length, F the force applied on the electron, q_0 the elementary charge and m_e the mass of the electron. The acceleration of the electron is:

$$a = \frac{U_{MCP} \cdot q_0}{l \cdot m_e} \quad (64)$$

The distance s an electron travels along the channel until it reaches the channel wall is:

$$s = \frac{1}{2}at^2 = \frac{U_{MCP} \cdot q_0 \cdot t^2}{l \cdot m_e \cdot 2} \quad (65)$$

With t the flight time of an electron until it hits the wall again. Assuming the initial velocity v_{init} of the initial secondary electron is perpendicular to the channel wall, the flight distance until it hits the opposite channel wall is the channel diameter d . t can be written as:

$$t = \frac{d}{v_{init}} \quad (66)$$

v_{init} can be derived out of the electron's initial kinetic energy U_{init} :

$$U_{init} = \frac{1}{2}m_e v_{init}^2 \rightarrow v_{init} = \sqrt{\frac{2U_{init}}{m_e}} \quad (67)$$

In inserting Eq.(66) and Eq.(67) in Eq.(65) leads to:

$$s = \frac{q_0 \cdot U_{MCP} \cdot d^2}{l \cdot 4U_{init}} \quad (68)$$

The energy U_c the electron gains during the flight time t is:

$$U_c = q_0 Es = q_0 \cdot \frac{U_{MCP}}{l} \cdot \frac{q_0 \cdot U_{MCP} \cdot d^2}{l \cdot 4U_{init}} \quad (69)$$

$$= q_0^2 \frac{U_{MCP}^2 \cdot d^2}{l^2 \cdot 4U_{init}} \quad (70)$$

The secondary electron emission coefficient δ is proportional to the square root of the energy U_c :

$$\delta = A \cdot \sqrt{U_c} = A \cdot \frac{q_0 U_{MCP} \cdot d}{2\sqrt{U_{init}} \cdot l} \quad (71)$$

With A a fit constant. After n collisions, the gain G_{ch} of one channel is:

$$G_{ch} = \delta^n = \delta^{l/s} \quad (72)$$

The number of collisions is the channel length l divided by the distance an electron flies within the channel before it hits the channel wall and ejects more electrons s . Inserting now Eq.(71) and Eq.(68) leads to:

$$G_{ch} = \left(A \cdot \frac{q_0 U_{MCP} \cdot d}{2\sqrt{U_{init}} \cdot l} \right)^{\frac{4U_{init}}{q_0 U_{MCP}} \left(\frac{l}{d} \right)^2} \quad (73)$$

By writing the channel length to diameter ratio $\frac{l}{d}$ as α and expressing the electrons initial energy U_{init} in [eV], the equation turns into:

$$G_{ch} = \left(A \frac{U_{MCP}}{2\alpha\sqrt{U_{init}}} \right)^{\frac{4 \cdot U_{init} \cdot \alpha^2}{U_{MCP}}} \quad (74)$$

With A in approximately $0.2 \left(\frac{1}{eV}\right)^{1/2}$, U_{MCP} in [eV], α is a dimensionless number and U_{init} in the range of a few [eV].

3 Setup

This chapter includes the stand of the NIM prototype as it was in January 2018 (Chap. ??). During test campaigns (Chap. bla) some parts such as the reflectron and the antechamber were exchanged and tested on the prototype. In May 2019 the tests with the NIM ProtoFlight Model (PFM) started. Chapter ?? describes the NIM PFM as it was at the beginning of the test campaign. During the tests, improvements had to be done such as adaptations of the ion source and improvements on the detector.

In Chap. 3.2 the test facilities are described. Tests with a neutrals particle beam were performed with the CASYMIR test facility at the University of Bern.

3.1 NIM Sensor Models

In this chapter, the NIM Prototype and the design of the NIM ProtoFlight Model (PFM) are described. The Prototype was build by Stefan Meyer and he also designed the NIM PFM [10]. The tests in Chapter 4 start with the configuration of the instruments as they are stated in this chapter.

Fig.27 shows the SIMION model of the Prototype ion-source Fig.28 shows the ion-source of the PFM and Fig.29 shows the filament housing of the Prototype (left) and of the PFM (right). The PFM has seven electrodes less than the prototype to simplify the source. Manly LV electrodes were taken together (IS 1& 2, IS 3 & 4, IS 6 & 7). IS 10 was removed and IS 11 was shifted towards the ionisation region. In the filament housing the filament electron repelling electrodes Fil 2-5 were taken together to one single repeller electrode Fil 2. The repeller electrode was splitted in 4 to compensate the filament position in case the filament was badly adjusted. For the PFM, the mounting of the filament holder was improved, therefore these 4 electrodes could be taken together to one single electrode.

Fig.30 shows a schematics of the ion-mirror. The prototype ion-mirror consists of 14 ring-electrodes (R2-R15). R1 is the drift tube. Between the electrodes R4-R15 are resistors to connect the electrodes with each other to generate a linear voltage gradient when a voltage is applied at electrode R4 and R15. In addition, a voltage can be applied on electrode R8 allowing additional focusing of the ions in the ion-mirror. The flight ion-mirror consists of a ceramic tube with two resistance spirals on its inner walls replacing electrodes R5-R7 and R9-R14. From the electrical point of view, the two ion-mirrors behave the same.

Ion-Optical System Prototype

Ion-Optical System Proto Flight Model

3.2 Test facilities/ Test Tools

3.2.1 Pumpstand nr. 2

Pumpstand nr. 2 was used to perform stand-alone tests with the different NIM detectors. The test setup consists of a vacuum chamber, a HV power supply, an oscilloscope, a computer to remote control the oscilloscope and a HV meter (Fig. 33).

We tested two different detectors from the electrical point of view.

During the further development of the detector, the diode in the detector was replaced by a resistor. To compare different measurements with each other it was required to determine the current flowing through the detector to determine the voltage over the MCPs. There are two different designs of the detector. One with a diode and one with a resistor

Fig. 34 shows the circuit diagram of the detector connected to an external power supply. Table 4 summarizes the used variables and gives a brief explanation.

The aim is to calculate the voltage over the MCPs U_{MCP} in dependence of the voltage difference U_{PSMCP} between the two outputs of the power supply U_{PSA} (anode output of the power supply for the detector) and U_{PSD} (MCP front voltage output of the power supply for the detector) as by the flight electronics the voltage U_{PSMCP} and the drift voltage U_{PSD} can be set.

$$U_{PSMCP} = U_{PSA} - U_{PSD} \quad (75)$$

The MCPs have a voltage depended resistance which implies that we need the current I_{MCP} flowing through the circuit to calculate U_{MCP} . As with the flight electronics it is not possible to measure this current, we do a calibration of the detector with laboratory electronics. This calibration is only valid when the detector does not come into saturation i.e. the current I_A is low compared to the current I_{RD} or the particle rate is below 10^6 particles/sec.

I_{MCP} is calculated by measuring the voltage over the test resistor R_M . U_A is measured with a high voltage meter. By substituting U_{PSA} with Eq.(75), I_{MCP} is then:

$$I_{MCP} = \frac{U_{PSMCP} + U_{PSD} - U_A}{R_M} \quad (76)$$

The voltage U_{PSMCP} can be written as:

$$U_{PSMCP} = U_{RM} + 2 \cdot U_{Ri} + U_{RD} + U_{MCP} \quad (77)$$

With $U_{Ri} = I_{MCP} \cdot R_i$ the voltage over the input resistors R_i , which are there to damp noise coupled into the detector circuit from the power supply. In the final tests it is about $100 \text{ k}\Omega$. U_{RD} is the voltage over the diode replacement resistor R_D . Further explanation about the improvement of the detector can be found in chapter bla. If the ion current I_{ion} is low, this results in a low anode current I_A :

$$I_A = G \cdot I_{ion} \quad (78)$$

with G the MCP gain. In this case $I_{MCP} = I_{RD}$ and:

$$U_{RD} = I_{MCP} \cdot R_D \quad (79)$$

Solving Eq. (77) to U_{MCP} results in:

$$U_{MCP} = U_{PSMCP} - U_{RM} - 2 \cdot U_{Ri} - U_{RD} \quad (80)$$

$$= U_{PSMCP} - U_{PSMCP} + U_{PSD} - U_A - 2 \cdot I_{MCP} R_i - I_{MCP} R_D \quad (81)$$

$$= (U_A - U_{PSD}) \cdot (1 + \frac{2R_i + R_D}{R_M}) - U_{PSMCP} \frac{2R_i + R_D}{R_M} \quad (82)$$

R_D	Resistor replacing the former diode	U_A	Voltage on the detector anode
R_i	Detector input resistor	U_{MCP}	Voltage over the MCPs
R_M	Resistor used to determine I_{MCP}	U_{PSA}	Anode voltage output of power supply
R_{MCP}	MCP resistance	U_{PSD}	Drift voltage output of power supply
R_T	50 Ω termination	U_{PSMCP}	Voltage difference between U_{PSA} and U_{PSD}
I_A	Current induced in the MCPs when an ion hits the MCPs	U_{RD}	Voltage over R_D
I_{ion}	Ion current hitting the MCPs	U_{Ri}	Voltage over R_i
I_{MCP}	Current flowing through the MCPs	U_{RM}	Voltage over test resistor R_M
I_{RD}	Current flowing through R_D		

Table 4: Variable list for the detector.

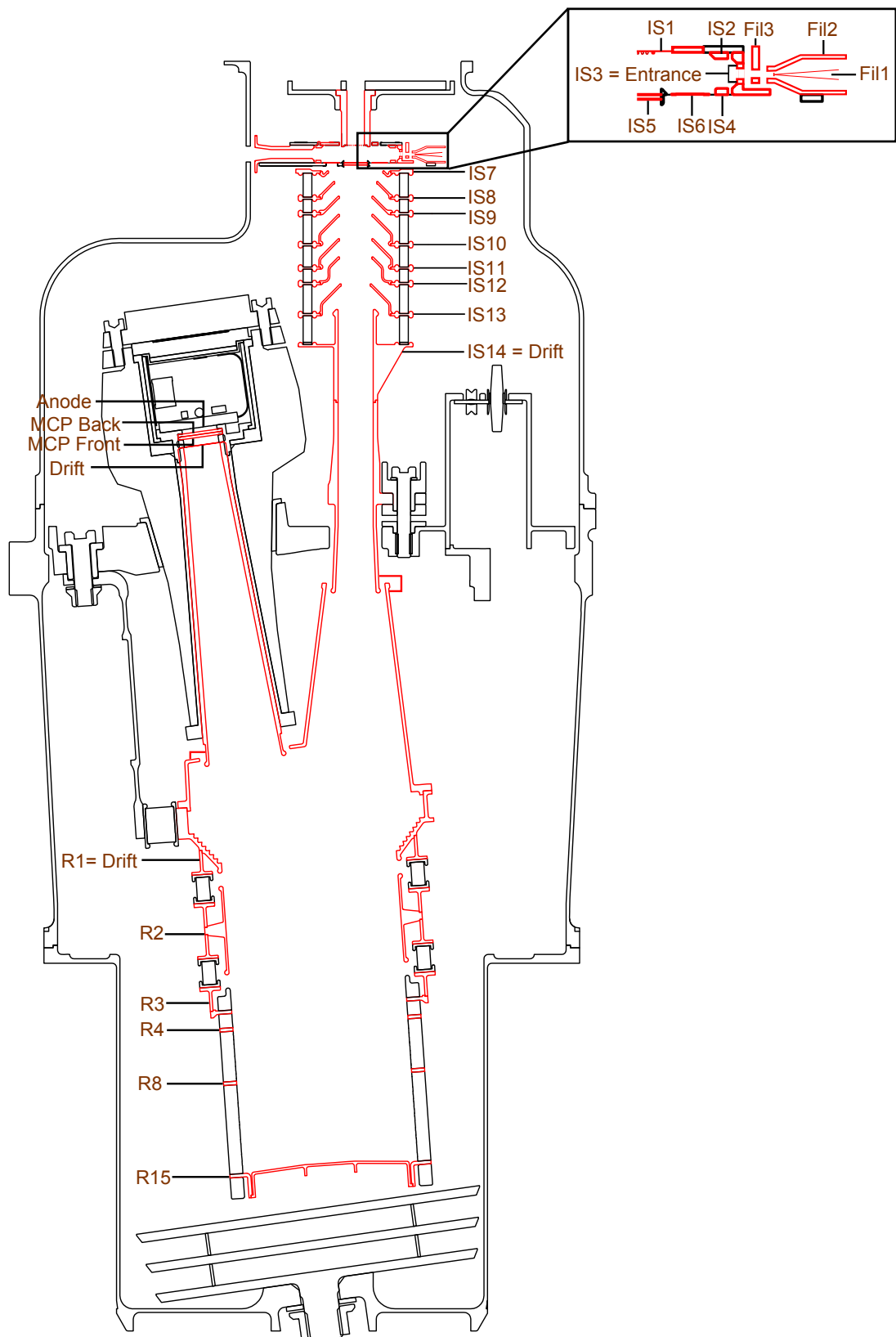


Figure 26: Schematics of NIM flight design with all electrodes marked in red.

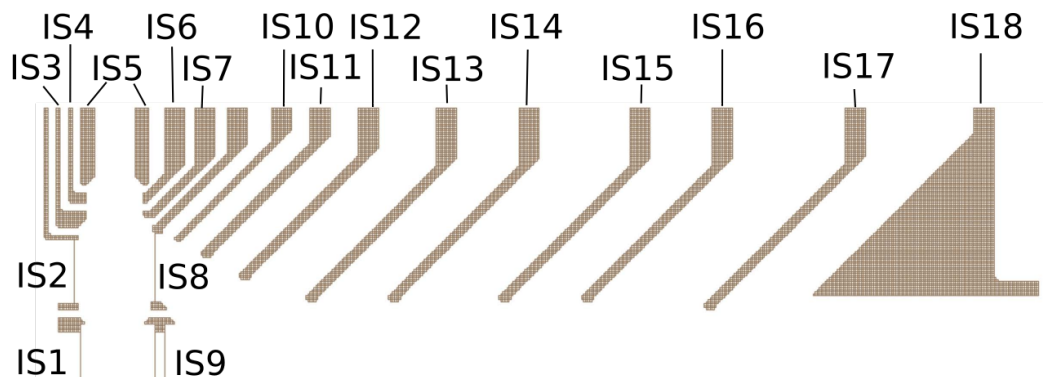


Figure 27: SIMION Model of the Ion-Source of the NIM Prototype [10].

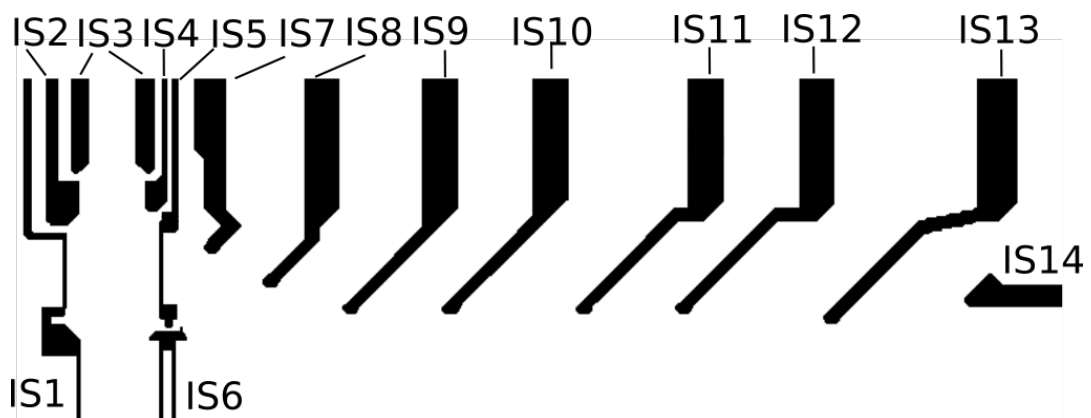


Figure 28: SIMION Model of the Ion-Source of the NIM ProtoFlight Model.

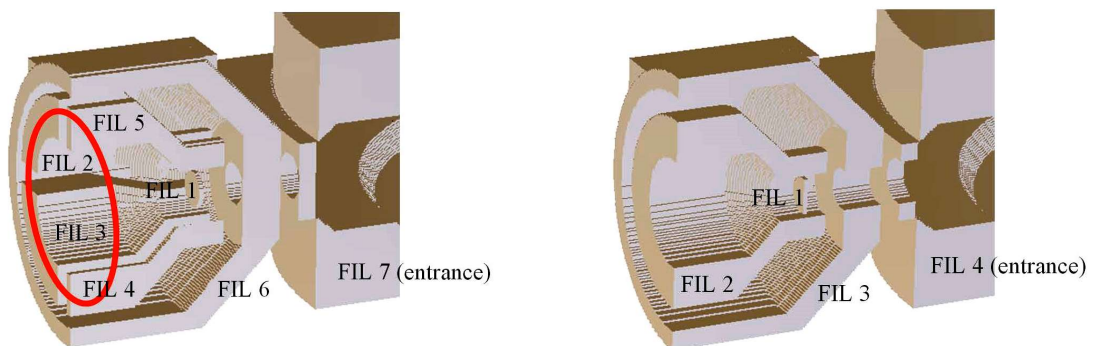


Figure 29: Left: Prototype filament housing. Right: PFM filament housing.

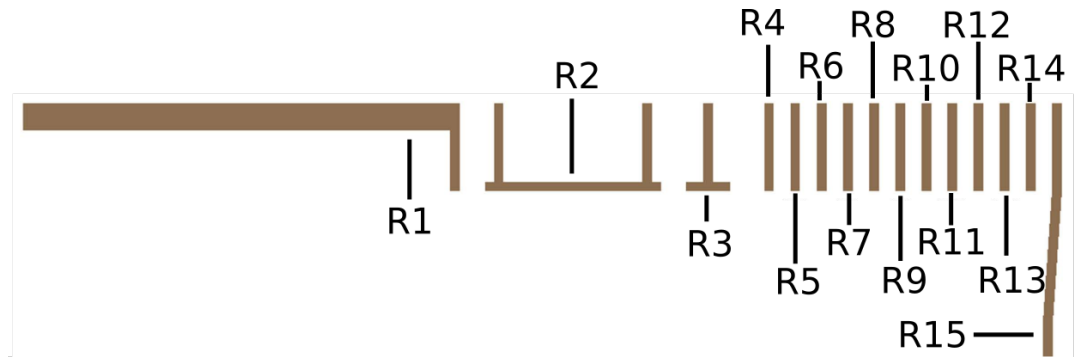


Figure 30: SIMION Model of the ion-mirror of the NIM Prototype [10].

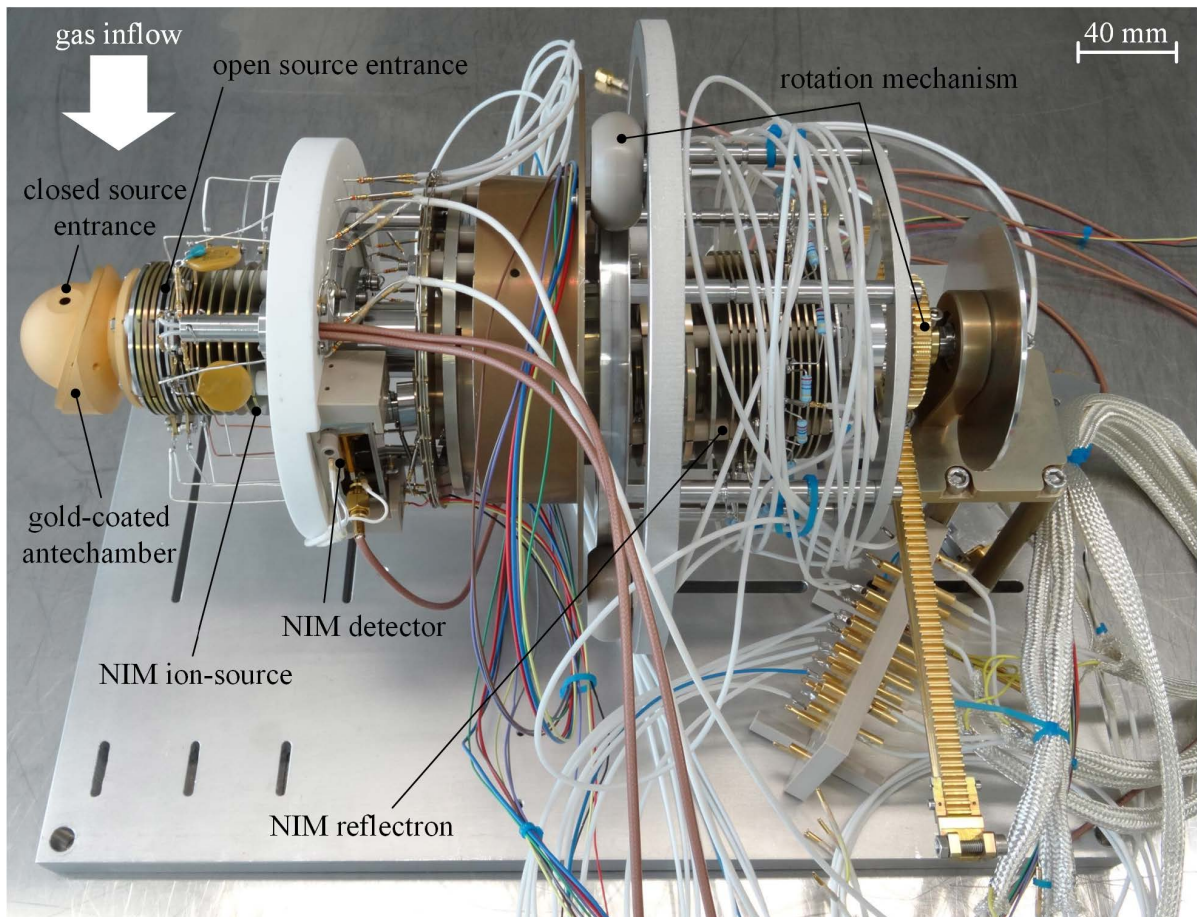


Figure 31: NIM Prototype [10].

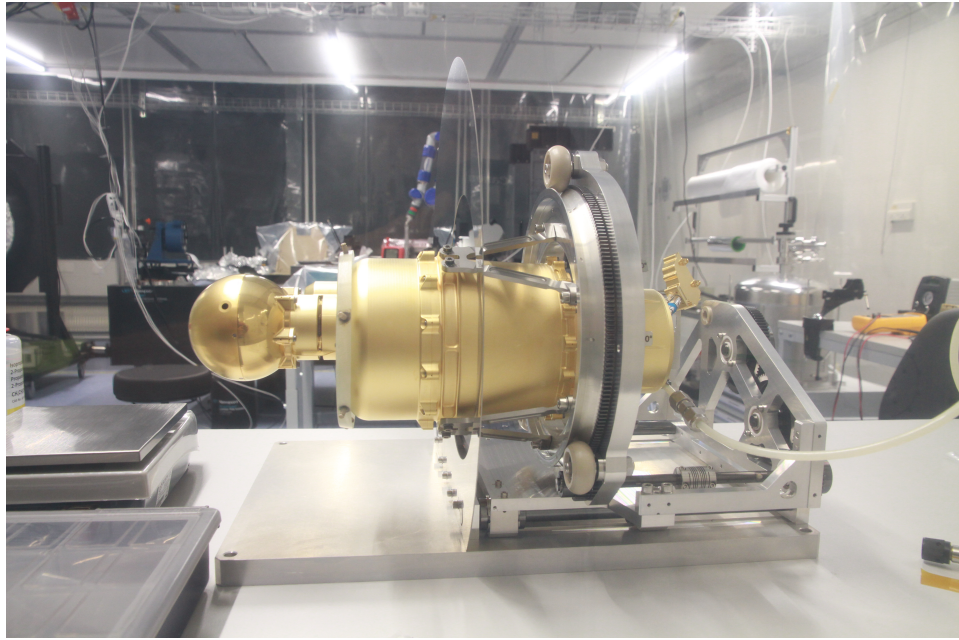


Figure 32: NIM PFM sensor head in calibration setup.

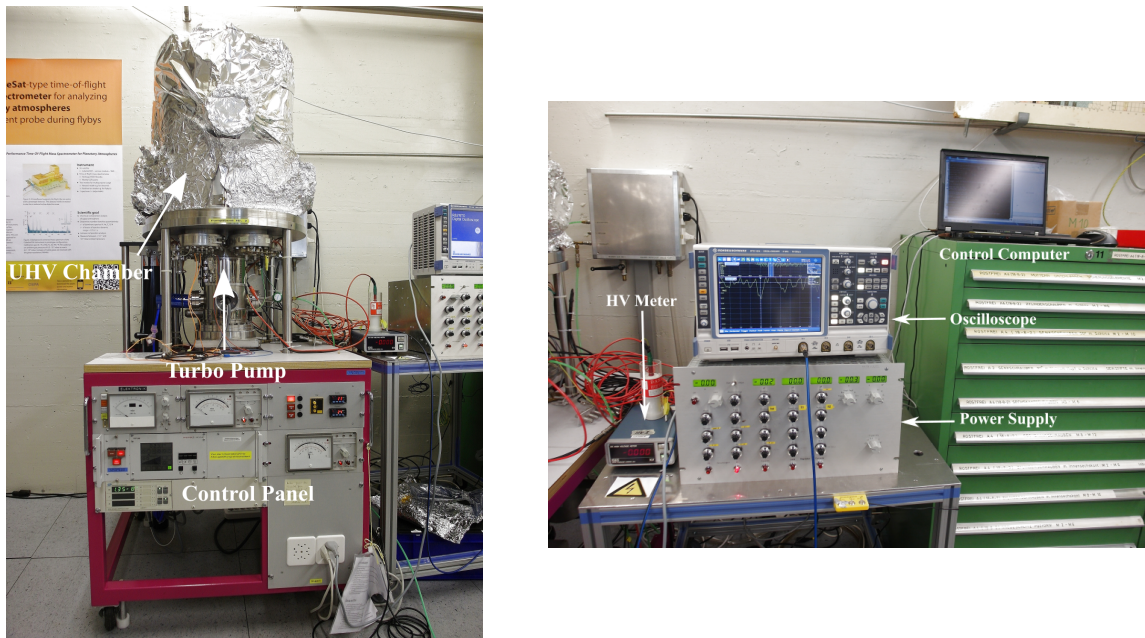


Figure 33: Left: Pumpstand nr. 2. Right: Power supply, oscilloscope and control computer for the stand-alone tests of the detector. The signal on the oscilloscope is a noise signal.

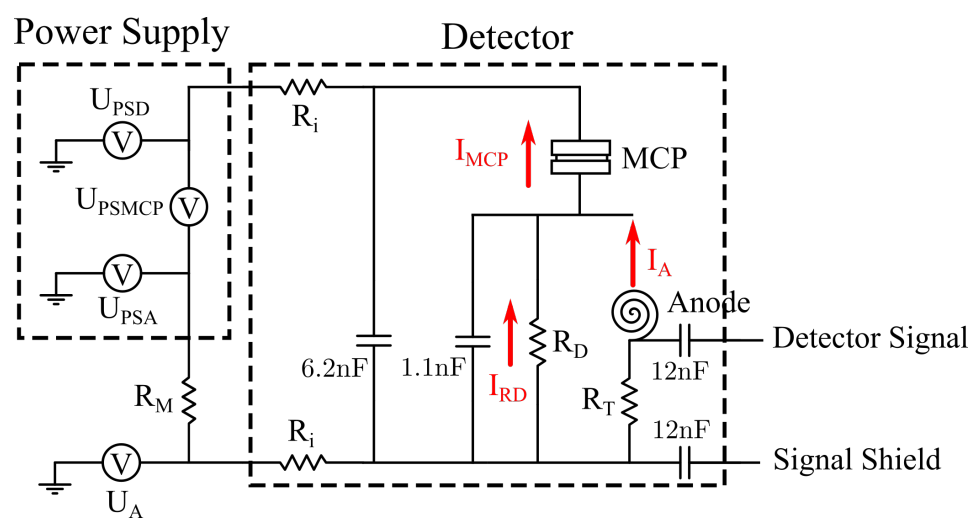


Figure 34: Electrical schematics of the NIM flight detector.

4 Experiments

The tests described in this chapter include tests of the different components of the NIM instrument such as laboratory tests of the flight antechamber tested on the Prototype or the flight ion-mirror. This part of Chapter 4 includes manly test with the prototype, and tests with the PFM and FS model.

In this section, the different tests are described to develop the NIM instrument. Different parts of the instrument were tested to improve the instrument.

4.1 Flight Ion-Mirror

In this section the performance of the two ion-mirrors is compared. As described in chapter 3.1, the prototype ion-mirror consists of several ring-electrodes connected with each other with resistors to generate a linear voltage gradient. The flight ion-mirror consists of a ceramic tube with two resistance spirals replacing some of the ring-electrodes. Fig. 35 left shows the prototype ion-mirror and Fig. 35 right shows the flight ion-mirror mounted to the NIM prototype in the test setup. An ion-mirror of the same type as the flight ion-mirror was also used in the RTOF mass spectrometer which flew in ROSINA [12] and the in the NGMS [6]. From the electrical point of view, the two ion-mirror types behave the same.

The measurements were performed in a vacuum chamber. The residual gas pressure for the

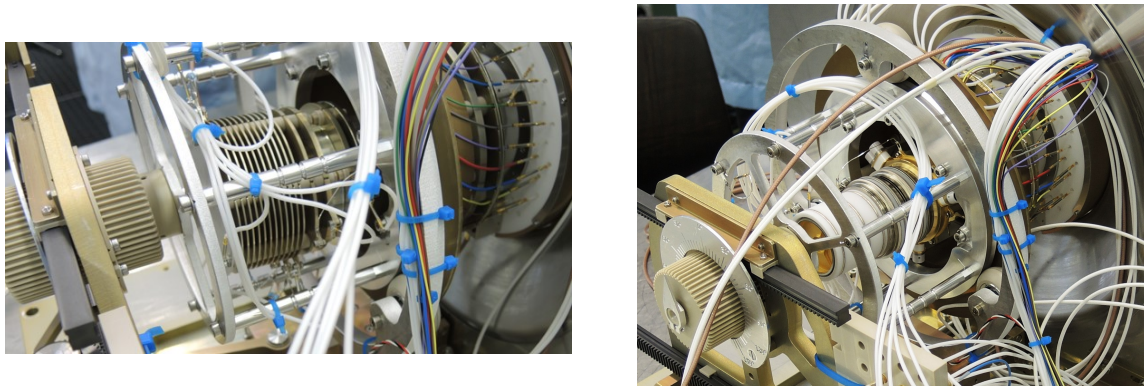


Figure 35: Left: Prototype ion-mirror with ring-electrodes. Right: Prototype with flight ion-mirror.

measurements with the prototype ion-mirror was $5 \cdot 10^{-10}$ mbar and for the measurements with the flight ion-mirror (PFMR) $1.4 \cdot 10^{-9}$ mbar. The test gases were injected directly through a leak valve to increase the chamber pressure up to $1 \cdot 10^{-8}$ mbar. The used test gases were: Ne, Ar, Kr and Xe. 3 Mio. single spectra were histogrammed for each of the measurements. All voltages of the instrument were optimized for the measurements with the two ion-mirrors. Table 5 shows the signal-to-noise ratios and the mass resolution of the different test gases measured with the two instrument configurations.

The SNR of the flight ion-mirror of the measurement with the flight ion-mirror is for all gases

Gas	SNR ProtoR	SNR PFMR	$m/\Delta m$ ProtoR	$m/\Delta m$ PFMR
^{20}Ne	2022.9	562.4	200 ± 12	236 ± 16
^{40}Ar	4732.6	1808.4	212 ± 9	267 ± 15
^{86}Kr	746.1	414.3	224 ± 7	292 ± 12
^{136}Xe	185.5	97.1	265 ± 8	332 ± 13

Table 5: Table listing the signal-to-noise ratios (SNR) and the mass resolution ($m/\Delta m$) of the prototype ion-mirror (ProtoR) and the flight ion-mirror (PFMR). The mass resolution in the table is underestimated to the real value.

lower than the SNR of the measurements with the prototype ion-mirror due to the higher amount of residual in the chamber during the measurements with the flight ion-mirror. The mass resolution of all of the test gases is higher when measuring with the flight ion-mirror.

4.2 Flight Antechamber

After successfully testing the flight ion-mirror, the flight antechamber was tested. A picture of the prototype and the flight antechamber is shown in Fig. 36. The antechambers consist of two parts. In the old design the two parts of the antechamber had a rim on which the screws at position $\pm 45^\circ$ were mounted to put the two parts together. Tests with this antechamber revealed that the neutral particles hit these screws and scatter into chamber (Fig. 37a) [11]. Therefore, an antechamber with a flat outer surface was required. In the new design the screws are recessed into the 1 mm thin surface of the antechamber to get rid of the needed rim in the old design. In addition the new antechamber is by a factor two bigger than the prototype antechamber with the aim to get more signal. Simulations of the flight trajectory revealed that two holes were required at positions $\pm 60^\circ$ to get optimal signal [1]. The CASYMIR test facility is not able to shoot the neutral particle beam under an angle of 60° onto the instrument. To test the new designed antechamber, an slightly different antechamber was used with the second entrance hole at position $\theta_0 = -90^\circ$ instead of -60° . With a rotation mechanism, the instrument can be rotated around the x-axes by $\pm 90^\circ$.

These measurements were conducted at the CASYMIR test facility at the university of Bern. CASYMIR is able to generate a neutral particle beam with velocities up to 5.5 km s^{-1} [3]. For these measurements the particle velocity was about 2.5 km s^{-1} because this is the velocity of the spacecraft in Ganymede orbit, which will be 90% of the measuring time of NIM.

Fig. 37 a) shows measurements conducted with the thermal mode when the old antechamber was attached [11]. For these measurements, the instrument was rotated around the x-axis by

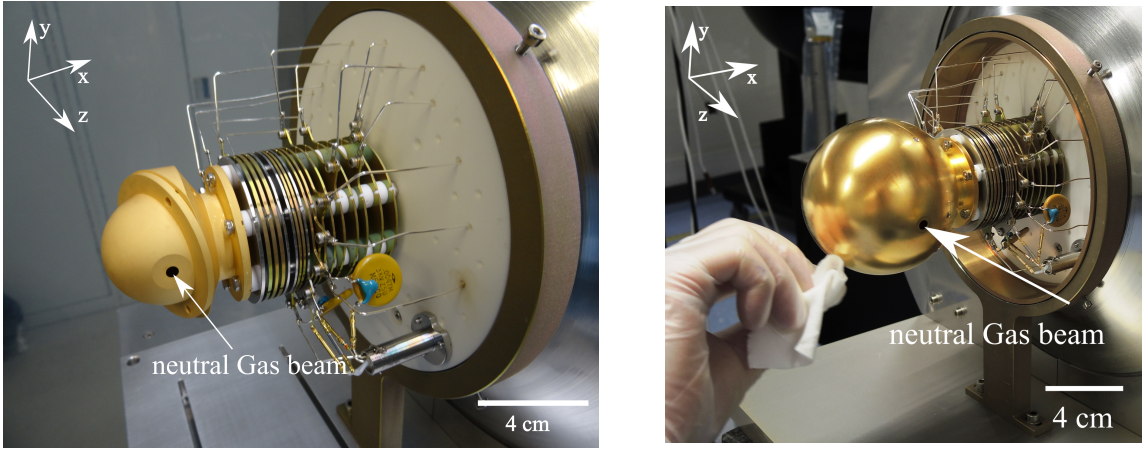


Figure 36: Left: Prototype antechamber. Right: flight-like antechamber with two entrance holes at positions $+60^\circ$ and -90° .

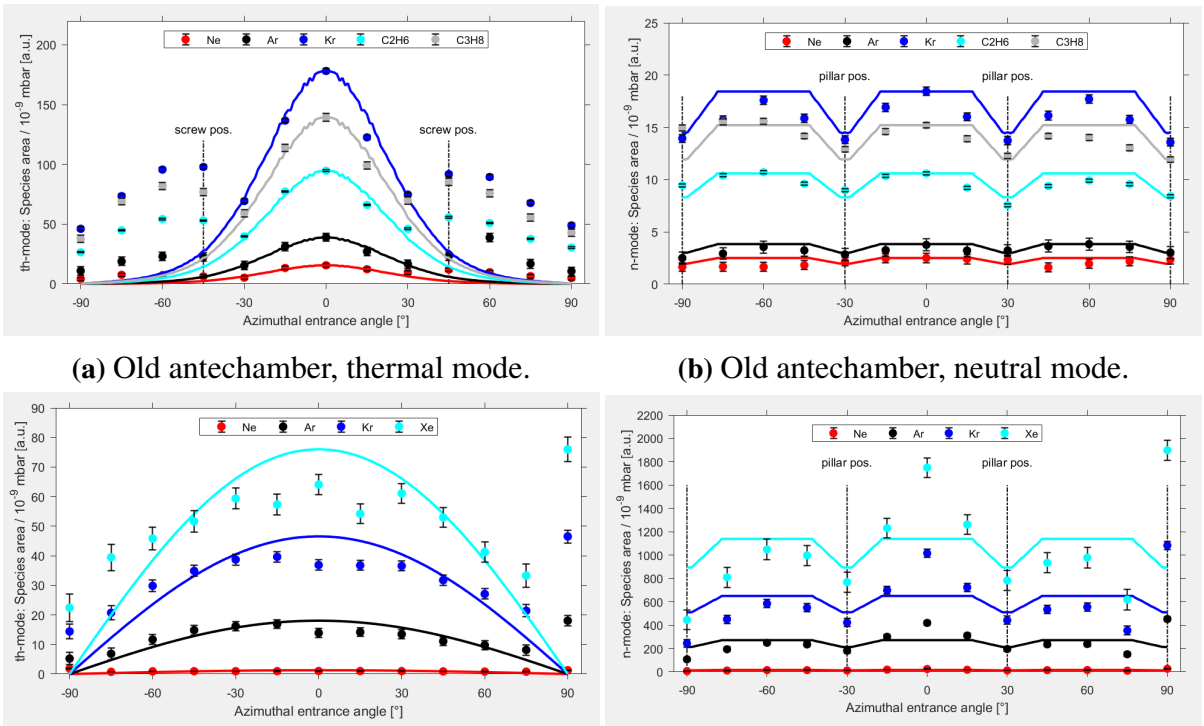


Figure 37: Panel a) and b) show measurements done with NIM Prototype sensor with the old antechamber attached. a) shows measurement conducted with the thermal gas mode and measurement of panel b) were conducted in neutral mode respectively [11]. c) and d) are the same corresponding measurements but performed with the new antechamber attached to the NIM instrument.

keeping the beam at the same position. When rotating the antechamber, the hole moves out the neutral particle beam because the beam is smaller than the antechamber. The expected intensity I_{ant} is the result of the function of the moving hole through the beam with a normal distribution:

$$I_{ant} = \frac{A}{\sigma\sqrt{2\pi}} \int_{x_{min}}^{x_{max}} \exp^{\frac{(x-\mu)^2}{2\sigma^2}} dx \quad (83)$$

With A a constant taking the beam intensity into account, σ the standard deviation of the beam and μ the position of the beam centre relative to the centre of the antechamber which is equal 0. The borders of the integral determine the part of the beam entering the antechamber:

$$x_{max} = r_{ant} \sin \alpha - r_{aHi} \cos \alpha \quad (84)$$

$$x_{min} = r_{ant} \sin \alpha + r_{aHi} \cos \alpha \quad (85)$$

With r_{ant} the radius of the antechamber and r_{aHi} the radius of the antechamber entrance hole. The sine contribution considers the shift of the hole in y-direction when the hole is rotated. The cosine contribution comes from the projection of the beam on the entrance hole. For the measurements with the new antechamber, the shift in y-direction when rotating the instrument was compensated by shifting the whole instrument. Therefore the sine contribution in Eq.(84) and Eq.(85) cancels out leading to a more cosine-like function.

When comparing Fig. 37 a) and b), we see that with the new design we successfully got rid of the artefacts previously induced by the mounting screws of the old design. The higher intensity at angle $+90^\circ$ is most probable an outlier because it appears in both the thermal (Fig. 37 b)) and the neutral mode graphic (Fig. 37 d)) of the measurements with the new antechamber. The drop in signal intensity when measuring with the thermal mode channel compared to the old measurements is a result of having two an additional entrance hole which was necessary because of the flyby trajectories (see Chap.2.3.3).

Fig.37 b) shows measurements conducted with the neutral gas mode with the old antechamber attached and Fig.37 d) shows measurements conducted with the neutral gas mode when the new antechamber was attached. At position $\pm 30^\circ$ and $\pm 90^\circ$ there are pillars holding the stack of the ion-optical lenses together. When the beam hits these pillars, the particles scatter in all directions leading to a damping of the signal. For the neutral gas channel, no difference in the signal distribution is expected because a change in the antechamber design does not influence the signal measured with the neutral gas channel. At 0° the signal is significantly higher than on the other plateaus. When shooting under this angle into the source, the neutral particle beam is in line with the electron beam leading to a higher signal. Another explanation is, that a different voltage set for the voltages in the ionization region changes the distribution of the electron beam thus leading to a different ion distribution in the ionization region. This leads to a different angular distribution of the signal for the neutral gas channel when comparing the results of the two measurement series. The difference in signal intensity also comes from the better voltage set. Some times its just enough to tune on the right electrode to get a signal amplification of a factor 2.
rewrite that explanation.

4.3 Entrance characterization

rewrite title.

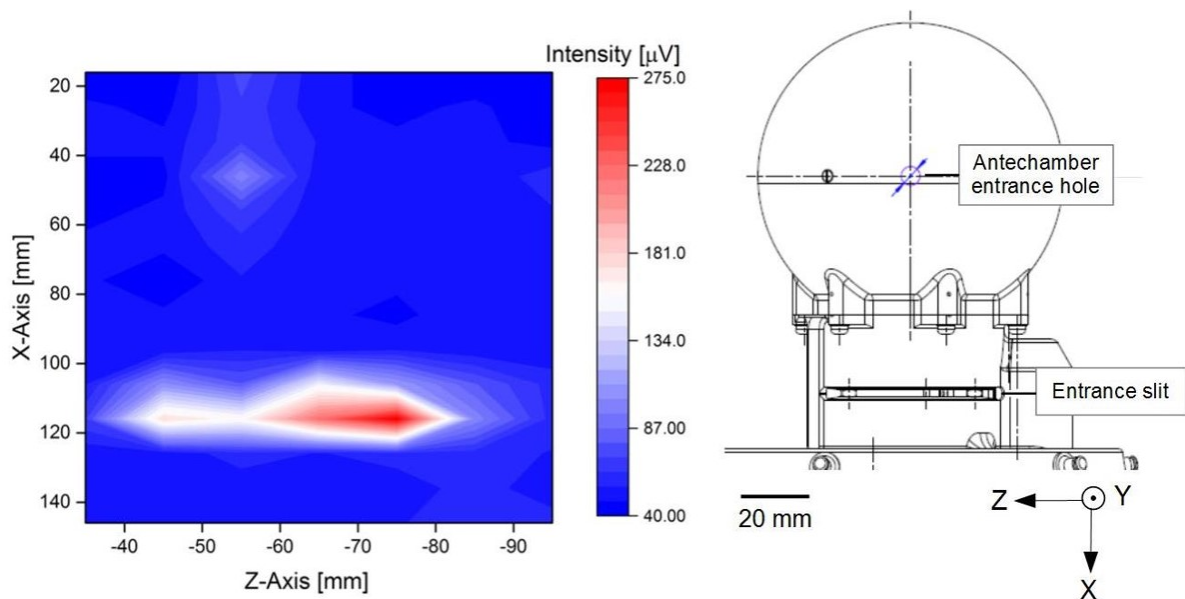


Figure 38: Left: Intensity profile when shooting with the neutral particle beam at the structure of the NIM PFM instrument. Right: Front view as seen by the neutral particle beam.

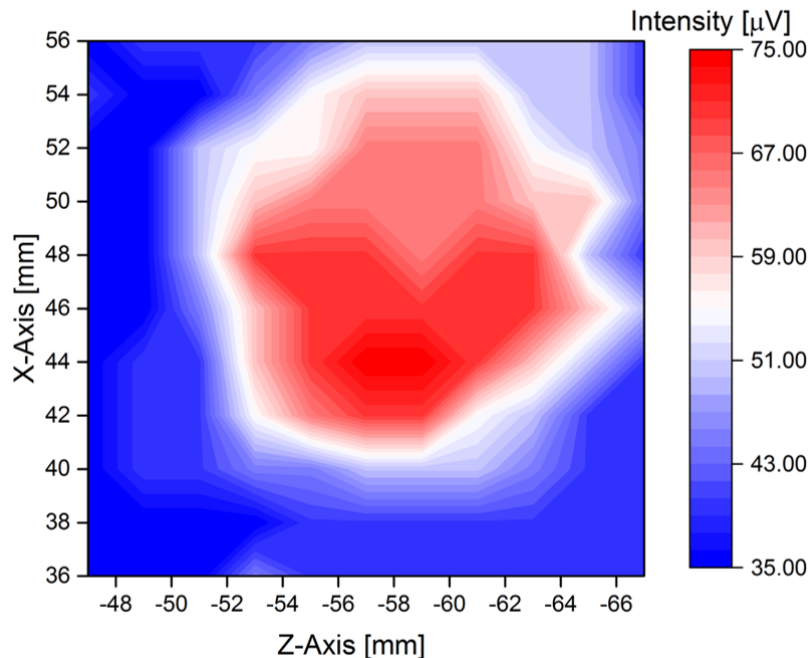


Figure 39: Zoom on the antechamber hole when shooting with the neutral particle beam at the structure of the NIM PFM instrument.

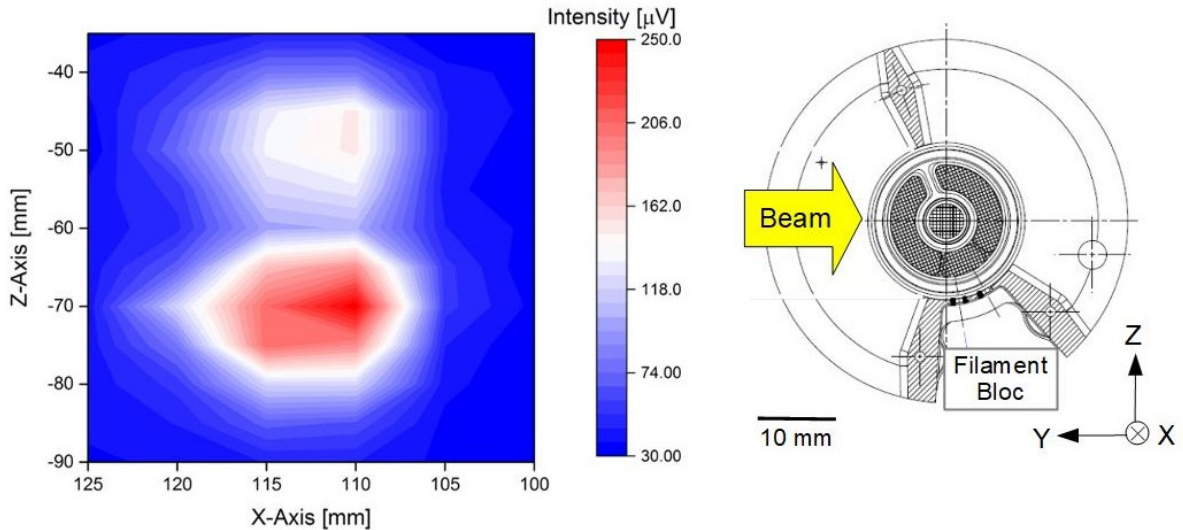


Figure 40: Zoom on the entrance when shooting with the neutral particle beam at the structure of the NIM PFM instrument.

For the first tests with the NIM PFM, the front side of the NIM instrument was scanned with the neutral particle beam to find the position of the entrance slit and the antechamber entrance hole to align the beam properly with the instrument. Fig. 38 left shows the scan of the front side and the right picture shows the corresponding structural part. The hole of the antechamber is clearly visible as a small dot. Fig. 39 shows a zoom with a better resolution of the antechamber entrance hole which shows a nice Gaussian distribution as expected. When looking at the entrance slit, there are two positions with increased intensities. The zoom on Fig. 40 reveals that the positions of biggest intensity is where the beam hits the structure covering the two electron emitting filaments. The other intensity maximum is where the beam hits the supporting structure opposite of the filament bloc. When the gas hits these structures, the gas slows down leading to a local increase of the gas density. Therefore, the structure partially thermalizes the gas similar as the closed source antechamber. This was not intended because with the neutral gas channel the aim is to measure incoming particles directly without any interaction with the structure. In the design of the PFM, the filament bloc and the supporting structure act like a funnel directing the sputtered gas to the central grid. The intensity amplification when shooting on the filament bloc is unavoidable. For the supporting structure opposite of the filament, a pillar instead of the plate like structure would have been the better option. When the gas hits the pillar, the pillar scatters the gas in all direction instead of scattering only in the direction of the central grid. This phenomenon was observed when doing a similar measurement with the NIM prototype (Fig. 41).

The ion-source of the prototype had six pillars holding the different focusing lenses together. In Fig. 41 the pillars are marked as red circles. The prototype had also an electron emitting filament. For these measurements, the ionization region was scanned with the neutral particle beam at angles 0° and $\pm 60^\circ$ to shoot between the pillars. When scanning from the front side, the signal intensity has a nice Gaussian shape. When shooting at angles of $\pm 60^\circ$ the Gaussian

distribution is visible when the neutral particle beam is aligned over the centre grid with an asymmetry toward the side of the filament. The filament bloc slows down the neutral particles leading to a small amplification of the signal. This amplification is less dominant than in the design of the PFM because the part of the filament structure seen by the beam is tilted outward. At distances bigger than ± 25 mm from the centre, the signal drops again. This is where the beam is completely outside of the ionization region.

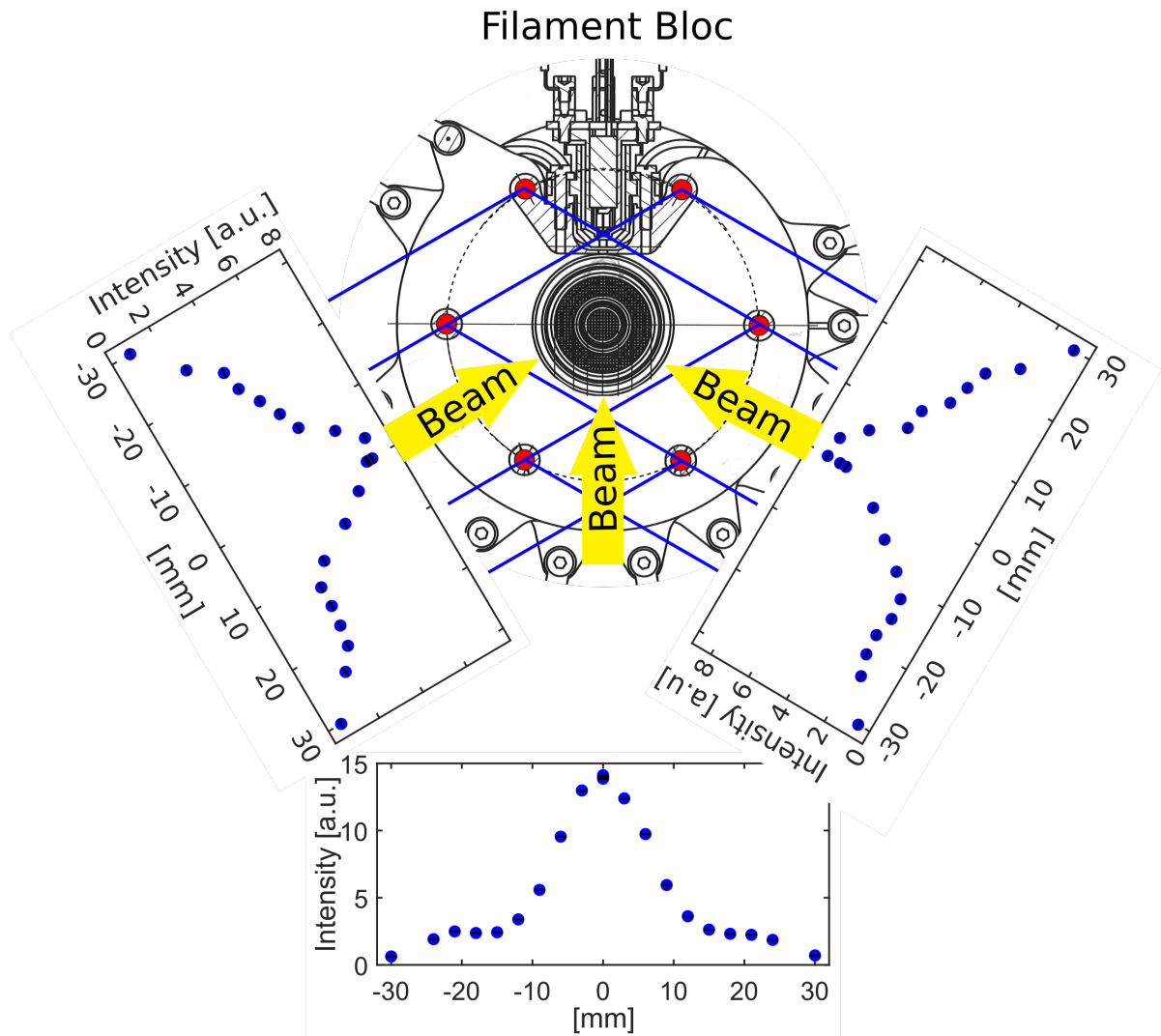


Figure 41: Zoom on the entrance when shooting with the neutral particle beam at the structure of the NIM Prototype. The red circles mark the positions of the pillars holding the ion source together.

4.4 Shutter Performance Test

When measuring with the neutral gas channel, the aim is that the particles are measured directly without any interaction with the structure of the instrument. Therefore, a shutter between the antechamber and the ionization region was required to close the particle entrance from the antechamber. In this section the performance of the shutter was tested. According to the model stated in Chap.2.3.5 the shutter should damp the signal by a factor 600.

These tests were performed with the NIM PFM Ref. as soon as the two models are properly described in the Setup section.. The PFM was operated with laboratory electronics. The tests were performed at the CASYMIR test facility. The used particle beam consisted of hydrogen and xenon with a velocity of 2 km s^{-1} . Three different measurements were performed: One with the beam directing onto the antechamber with the shutter open, one with the shutter closed and a background measurement, where the particle beam was pointed onto the outer structure of NIM to estimate how much of the signal arises from the test gas scattering into the ionization region when the beam is directed in an arbitrary direction. This background was subtracted from both signals before they were divided through each other to determine the damping factor G_{close} of the shutter.

The damping factor of the shutter according to the measurements is 12 instead of the required 1000. The biggest impact has the actual thickness of the gap between the shutter and the antechamber when the shutter is closed. The damping reduces significantly when the gap is bigger than actually designed. This is shown in Fig. 24 in Chap. 2.3.5. With a gap size of about 0.1 mm instead of 0.01 mm the damping factor is only about a factor 25. Other reasons are that the portion of the beam which scatters on the antechamber outer walls gets thermalized in the vacuum chamber and adds to the signal intensity. In the outer space, the gas scatters on the antechamber but does not reach the ionization region because it will flow around the instrument.

4.5 Simulations

During development, the mounting of the HV lenses was adapted. Simulations had to be done because as a result of the changed form of the lenses, the voltage set also changed. In this case, the voltage ranges increase by about blabla volts. These new higher ranges challenged the design of the supply electronics because the electronics has a limited amount of space.

4.6 Filament decision

4.7 Pulser

The high voltage pulser is used to accelerate the generated ions in the ionisation region to a certain energy. During the time when no high voltage pulse is applied, the potential has to be stable at the bias voltage to allow ion storage as previously discussed in chapter 2.3.2.

Fig. 43 shows a schema of a realistic high voltage pulse and Table 6 shows the characteristics

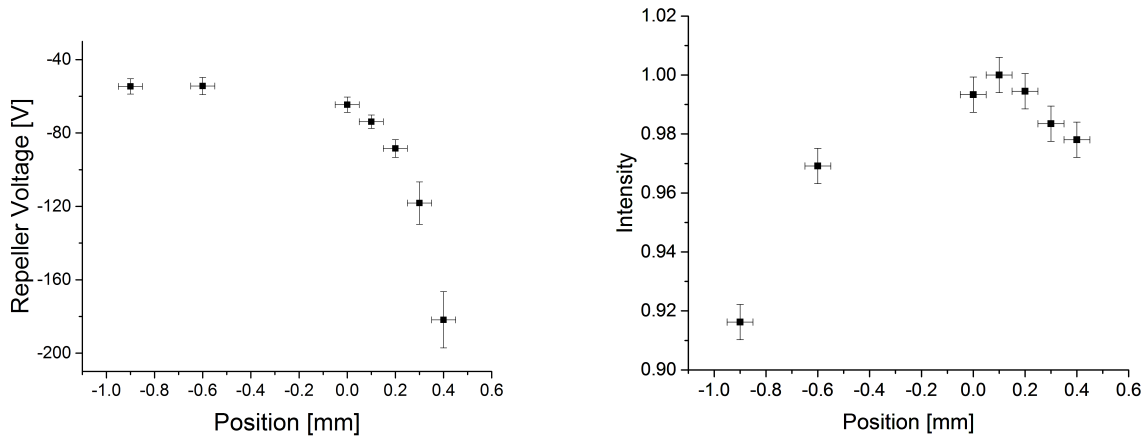


Figure 42: Left: The filament repeller voltage to reach the maximum electron intensity over the volume of the neutral particles. Right: Electron intensity normed on the intensity at position 0.

of the flight pulser compared to the requirements. The fall time is the time to build up the negative high voltage. This time has to be very short to give all particles the same amount of energy. With a thickness of the ion-source of 2 mm and a voltage of -480 V, atomar hydrogen needs about 3 ns to leave the source. Helium needs already 6.5 ns. To affect as few species as possible but to set a realistic requirement, the maximum fall time of the high voltage pulse has to be smaller than about 5 ns. The fall time of the flight pulser slightly exceeds the that value with a fall time of 5.76 ns. Therefore it still only affects hydrogen. When applying a high voltage, the pulse overshoots its set value and drops slightly. The overshoot and the voltage drop result in a variation of the particle energy for the different species. The ringing of the high voltage, and the pulse drop of the flight pulser are within the specifications. The pulse duration has to be longer than $0.2 \mu\text{s}$ because that is the minimum time particles with masses of 1000 u need to leave the ionisation region. With some margin, the specifications were set to $0.5 \mu\text{s}$. The rise time to bias voltage should be smaller than 100 ns to leave enough time for ion storage. This is well achieved with the flight pulser. The ripple of the bias voltage should be smaller than $\pm 50 \text{ mV}$ to generate a stable electric field for ion storage in the ionisation region during the time when the high voltage pulse is not applied. This ripple should be smaller than $\pm 50 \text{ mV}$. However, the flight pulser exceeds this value. How big the impact actually is, is difficult to estimate. But due to limited choices for the different components of the pulser, this pulser is the best which we were able to produce with the available resources. A further discussion about the design decisions and the requirements for the available components can be found in [7].

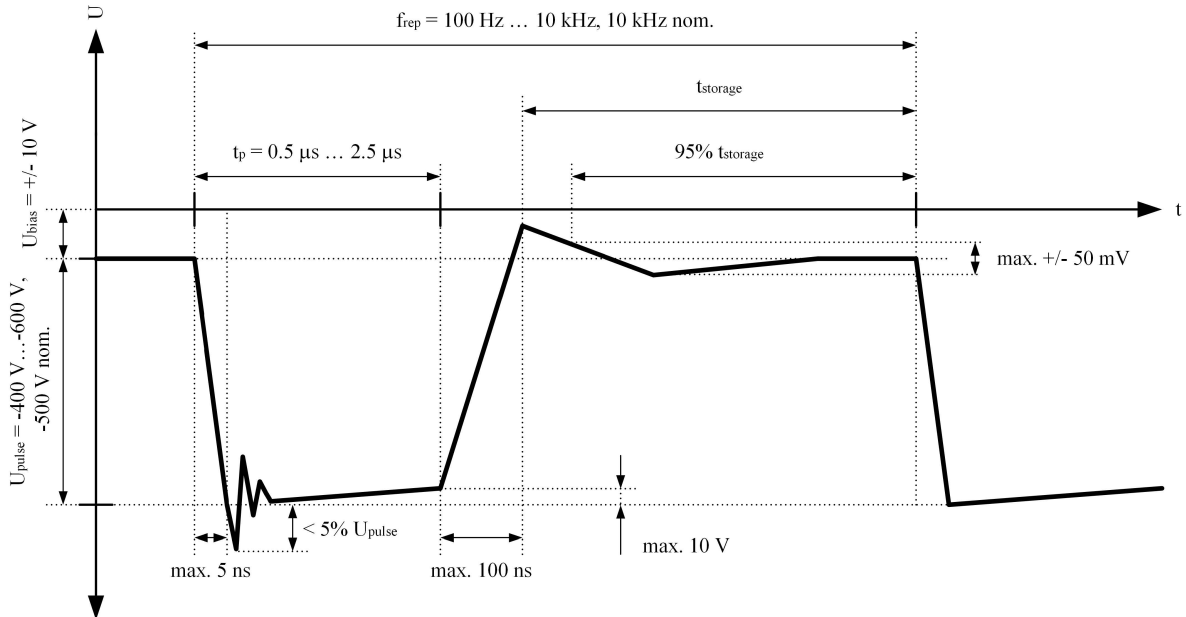


Figure 43: Specifications for the pulse shape generated by a realistic pulser [10].

	Ringing of HV Pulse	Pulse drop at full HV	Baseline Ripple	Fall Time	Rise Time
Requirement	< 5%	< 10 V	$\pm 50 \text{ mV}$	< 5 ns	< 100 ns
Flight Pulser	2.5%	1.9 V	300 mV	5.76 ns	19.7 ns

Table 6: Characteristics of the flight pulser compared with the requirements.

4.8 Detector Tests

The following chapter describes improvements of the mechanical and electrical design of the NIM PFM detector and tests performed with different versions. Most of the tests were performed in the Pumpstand nr.2 (Chapter 3.2.1) and a few were done with the detector in the sensor Proto Flight Model (PFM) or in the sensor flight spare model (FS).

The detector suffered repeatedly discharges causing a failure of the diode, which is one of the key components of the detector. This lead to a redesign of the detector housing and to an exchange of the diode through a resistor, because the resistor is more robust concerning discharges. The discharges could be eliminated by a redesign of the detector housing. Fig. bla left shows an earlier version of the detector housing and Fig. bla right shows the design of the current flight detector. Basically, the MCPs lay on a border about 1 mm above the anode. A diode generates an additional voltage difference between the MCP backside and the anode to accelerate the electrons from the MCP backside towards the anode. Between this border

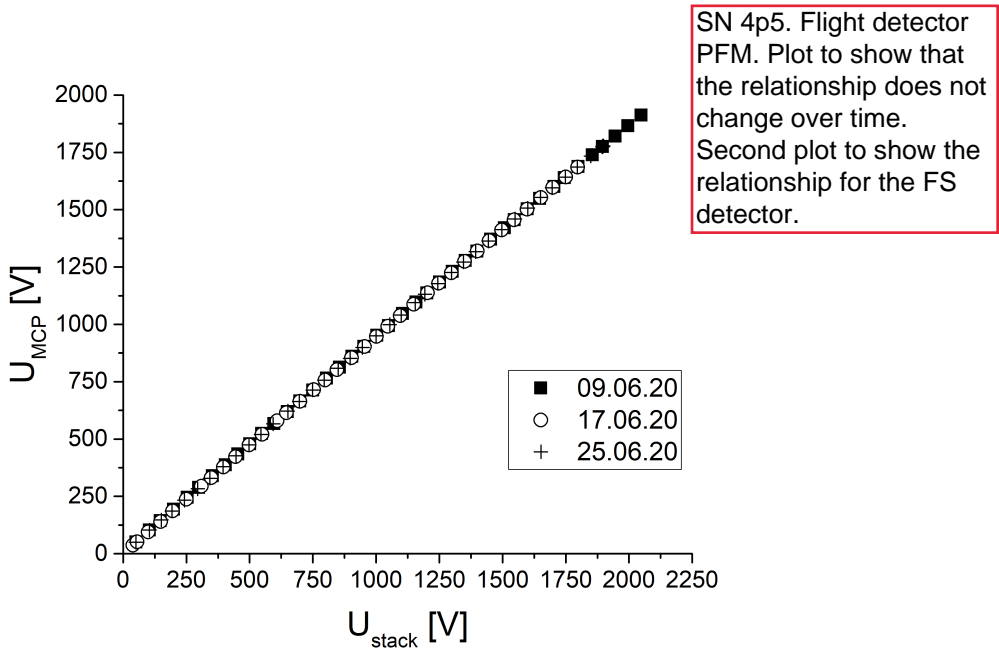


Figure 44: Dependence of the MCP voltage (U_{MCP}) from the voltage applied over the detector (U_{stack})

and the MCP is the contact lug which is connected to the high voltage rail. On top of the upper MCP is the contact lug to connected to the corresponding voltage rail. On top of that is a bushing and a sort of screw. When tightening the screw, the bushing presses uniformly on the MCPs. In the old design, the thread for the screw was cut down to the boarder on which the MCPs lay. When assembling the whole stack, the MCPs often cant in the thread. Another challenge lay in tightening of the screw. When the screw was too loose, the top and the bottom contact lug had no reliable contact to the MCPs. When applying a high voltage over the whole MCP stack, the gap acts as an additional resistor over which the voltage build up resulting in a discharge between the corresponding electrode and the MCP. The discharge can propagate through the whole MCP stack and damage the diode and the capacitors. When the screw was tighten too much, the MCPs broke as they consist of lead glass and are very delicate in the mechanical point of view. As a consequence, the screw thread was cut less deep down and an additional boarder was made on which the bushing was pressed by the screw to make the assembly of the detector easier. In addition, the diode was exchanged through a resistor because the resistor is more robust in regards to the discharges. Due to the uncertainty in the manufacturing process of the detector housing, spacer rings are added between the bushing and the MCP to really close the gap. Due to that uncertainty, the number of rings needed for each detector has to be determined by trial.

Fig. bla shows the signal shapes of different detector configurations beginning with the shape of a detector with a broken diode. The other two figures show the signal shape of a detector with a functioning diode and a functioning resistor. The most remarkable feature is that the signal height of the detector is much smaller and much broader than the signal shape of the

other two configurations. In addition, the first overshoot is much larger due to the impedance mismatch caused by the broken diode. A broken diode gets conductive and therefore the potential at the MCP backside is equal to the potential of the anode. The electrons are not additionally accelerated and therefore the resulting signal is smaller than the signal with a functioning diode.

Fig.45 shows the gain curves of two potential FS detectors both in the configuration with a $10\text{ M}\Omega$ resistor instead of a diode.

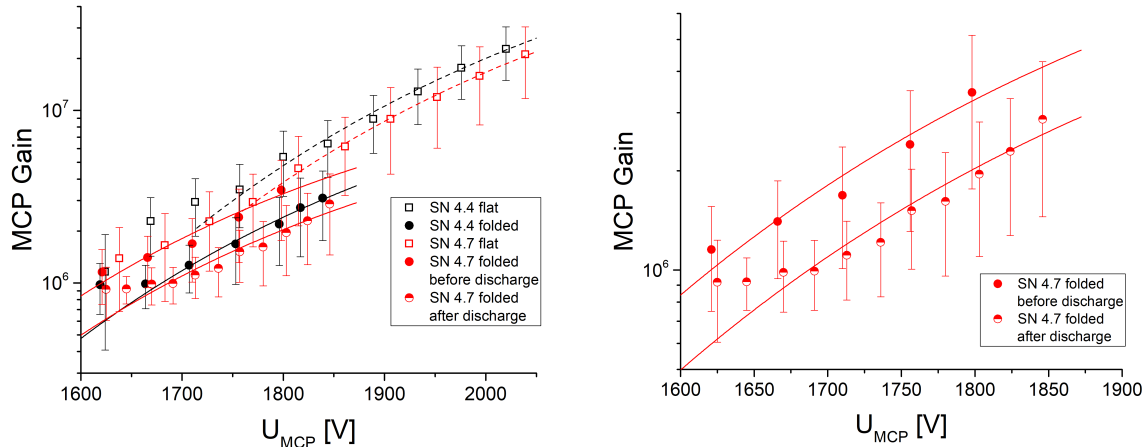


Figure 45: Left: Gain curves of two NIM PFM detectors. The difference in gain is because for each measurement curve, a different set of MCPs was used. Right: Gain curves of a folded NIM PFM detector. The lower gain curve was recorded after a discharge at an MCP voltage of 1.8kV.

4.9 Ionoptics

Delete that chapter.

4.9.1 Voltage Optimisation

Two types of electrical lenses. positive and negative voltage lenses. positive and negative voltage lenses have the same effect. In negative voltage lenses, the particles fly faster = shorter time-of-flight. This results in a better mass resolution.

Aim in the lab is to get two different voltage sets. One for positive voltages to not stress the equipment and one with negative voltage lenses to reach the maximal performance of the instrument. -; Tests showed no significant better mass resolution. A more detailed data analysis has to be made.

4.10 Instrument performance tests

4.10.1 Prototype

Prototype is part of the instrument development. Therefore, these test are part of the previous sections. This chapter will be deleted here. PFM and FS make sense to be treated specially thus there are measurement campaigns with the whole instruments.

4.10.2 PFM

4.10.3 FS

Ion Storage two different velocities

Ion storage is very crucial for a time of flight mass spectrometer because every ion generated and not stored in the ion source is lost and can generate additional electrical noise on the detector signal line. In this test the ion storage behaviour of the ion source was analysed for thermal and neutral mode for hydrogen and krypton with velocities of 2 km s^{-1} and 4 km s^{-1} . The emission current was varied from 20 to $600 \mu\text{A}$. Ion storage of positive ions in x- and y-direction is supported by the negative potential generated by the electron beam. Two ring electrodes with a positive voltage applied generate a positive potential ring to trap generated ions in y- and z- direction (Fig.46). For emission currents from 20 to $600 \mu\text{A}$ according to Eq. (35) the negative potential in the centre of the electron beam is -0.08 - (-2.59) V. Fig.47 left shows the ion storage behaviour of the ion source of hydrogen and right the ion storage behaviour of krypton. In case of no ion storage, the relationship between the electron emission current I_{em} and the signal intensity is linear. In case of ion storage there is a quadratic relationship between I_{em} and the signal intensity. When measuring with the thermal mode, the particles get slowed down until they have energies in the range of 0.01 eV and are therefore easy to trap in the potential field. In neutral mode particles enter the ionisation region directly. The kinetic energy of hydrogen for velocities between 2-4 km/sec is 0.07-0.27 eV. It can therefore easily be trapped in the potential field by the electron beam and the potential of the ring electrode already with very emission currents as low as $20 \mu\text{A}$.

The kinetic energy of ^{84}Kr for the same velocities is 2.8-11.2 eV. This energy exceeds the potential of the centre of the electron beam and the ions are therefore more difficult to trap with only the electron beam. The ions are kept in the middle of the ionisation region with the positive potential ring. According to Fig. 47 ion storage for ^{84}Kr starts to dominate at emission currents of $100 \mu\text{A}$. In thermal mode, an increase in beam velocity leads to an increase in signal intensity due to the density enhancement effect (Ref.). Therefore a higher signal intensity is expected in thermal mode for 4 km s^{-1} compared to 2 km s^{-1} . Like the in PFM, the FS shows a nice ion storage behaviour. For krypton ion storage just starts at an emission current of $100 \mu\text{A}$ where hydrogen is stored already at lower emission currents due its lower kinetic energy at the same beam velocity.

Mass resolution and Signal-to-Noise Ratio

According to the requirements stated in (Ref.) the required mass resolution for neutral mode is 500 and for thermal mode it is 1000 m/dm but to be able to distinguish between different masses at unit masses of 1000 u NIM has to have a mass resolution of 1000. Otherwise NIM the different unit masses cannot be distinguished. Fig. 48 show two spectra recorded with the NIM flight sensor with laboratory electronics attached with an electron emission current of

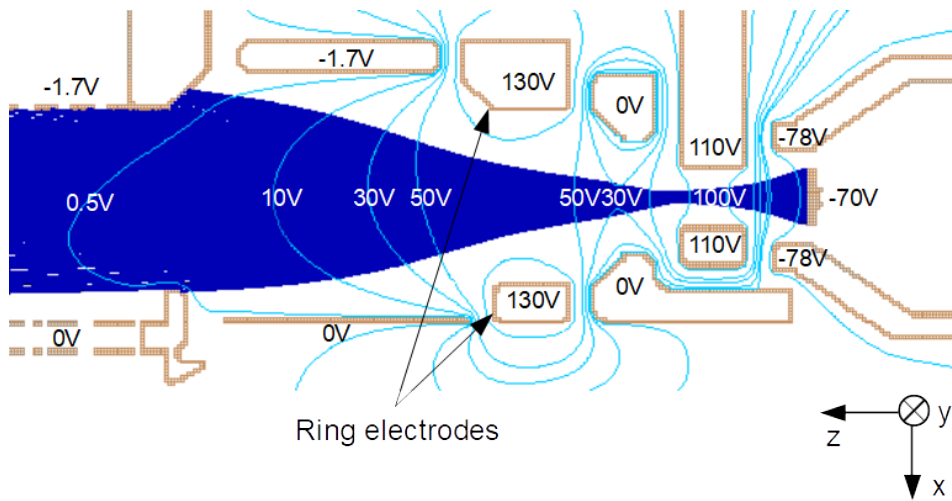


Figure 46: Ion storage source with sample voltage set applied to the electrodes. In light blue are the potential lines and in dark blue a simulated electron beam.

100 μ A. With a mass resolution of 708 for neutral gas mode NIM fulfils the requirements. In thermal gas mode the highest mass resolution achieved was $830 \text{ m}/\Delta m$ which comes close to the requirements. Fig. 49 show the mass spectra recorded with the NIM flight sensor with the flight electronics attached. The electron emission current was 200 μ A the highest mass resolution achieved at the current state is $490 \text{ m}/\Delta m$ for neutral gas mode and $462 \text{ m}/\Delta m$ for thermal mode. Fig. 50 shows a mass spectrum recorded in thermal mode with an emission current of 300 μ A the ^{78}Kr peak is clearly visible. The signal to noise ratio for the spectra recorded with the flight electronics is very low compared to the SNR for the spectra recorded with the laboratory electronics. We also observe noisy part wandering between the single spectra. There is a significant part of repetitive noise appearing not always at the same position in the spectrum. With a proper noise filter this noise can be detected and significantly reduced without affecting the mass signal peaks. For future work, there is a lot of potential for improving the spectrum by proper analysing the noise and writing filters to suppress the noise. Fig. 51 shows a mass spectrum recorded with the flight sensor with the laboratory electronics attached. The highest SNR achieved was $6 \cdot 10^5$ and therefore almost 6 decades. The mass peaks 355 u, 390 u and 429 u are some oil components with water adducts coming from the used turbo pumps of the test facility. 415 u is an artefact coming from the background subtraction algorithm. The artefact peak is also wider then the other surrounding mass peaks.

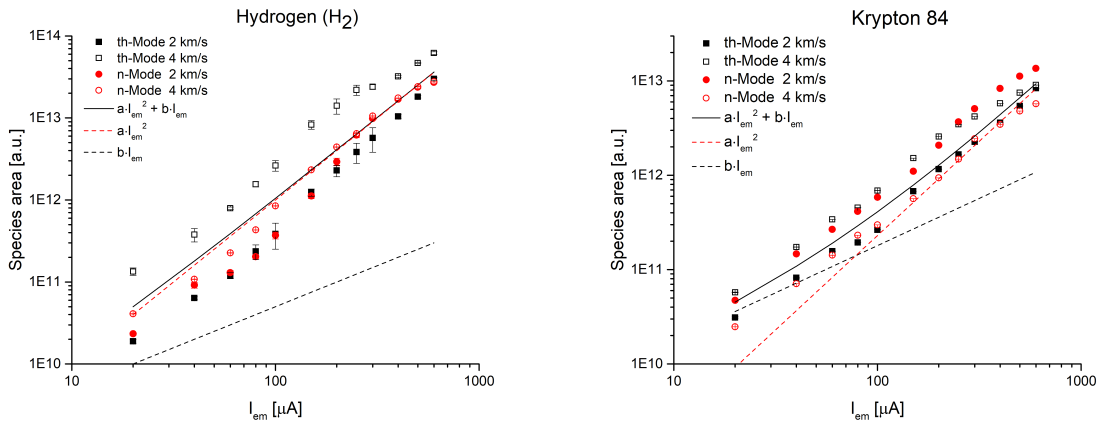


Figure 47: Ion storage measurement with the flight spare sensor but with laboratory electronics attached for H_2 and ^{84}Kr for two different gas velocities.

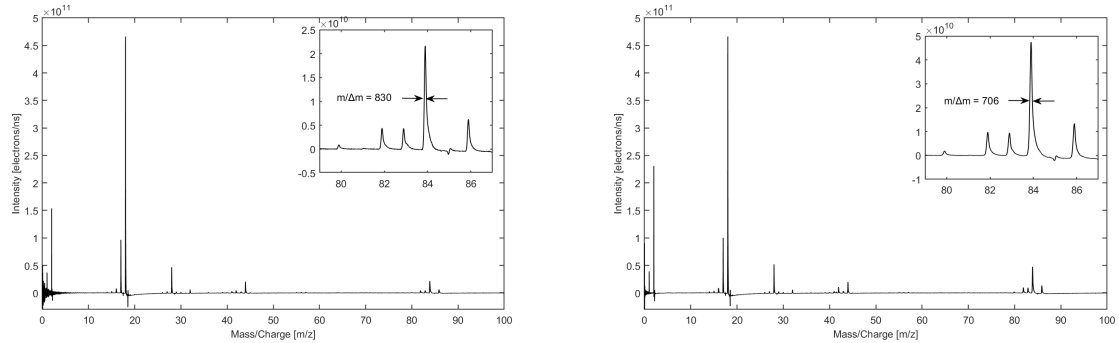


Figure 48: Mass spectra measured with the flight spare sensor with the laboratory electronics attached. Left: with thermal gas mode Right: neutral mode.

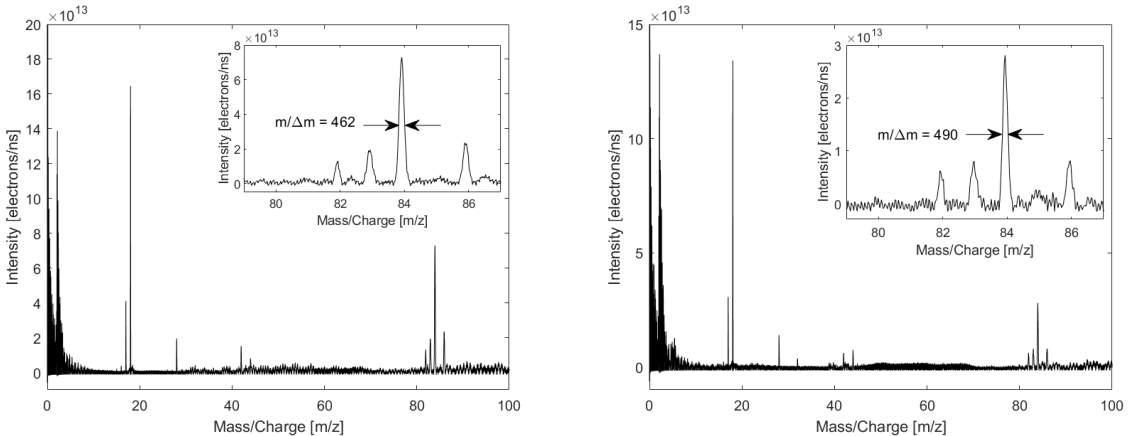


Figure 49: Mass spectra measured with the flight spare instrument with the flight electronics attached. Filament emission current was 200 μA . Left: with thermal gas mode Right: neutral mode.

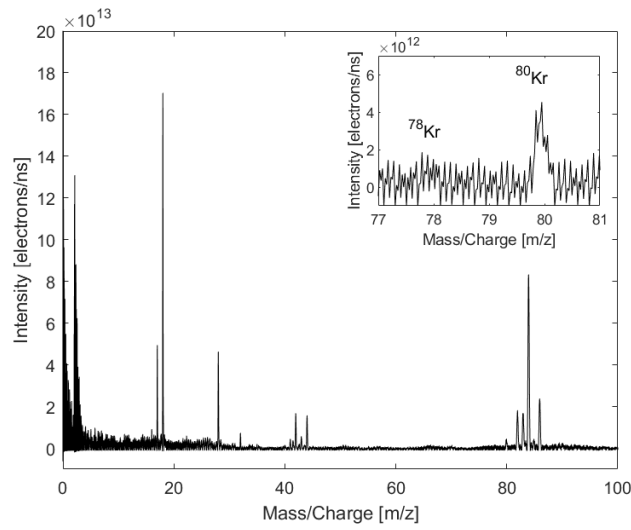


Figure 50: Mass spectra measured with the flight spare instrument with the flight electronics attached. Filament emission current was 300 μA .

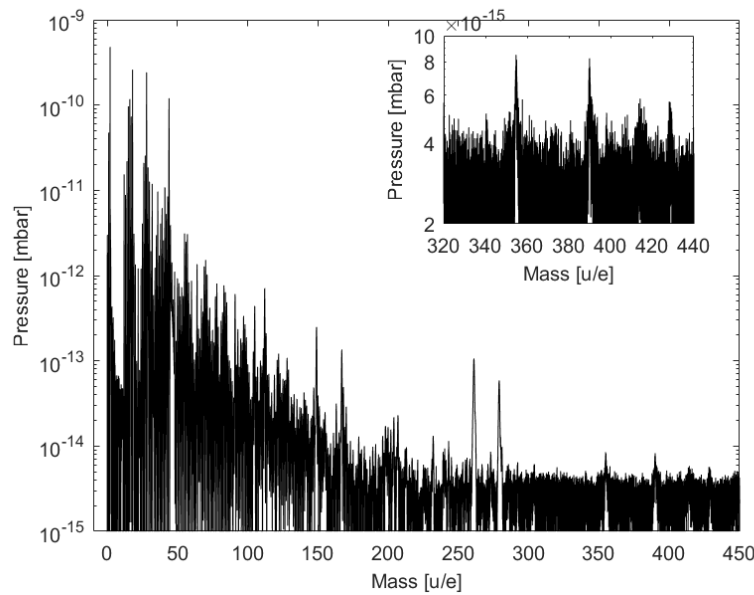


Figure 51: SNR plot for the flight spare sensor but with laboratory electronics attached at a chamber pressure of $1.5 \cdot 10^{-9}$ mbar.

5 Conclusion

6 Outlook

References

- [1] A. Boutonnet and G. Varga. JUICE- Jupiter Icy moons Explorer Consolidated Report on Mission Analysis (CReMA), esa document jui-esoc-moc-rp-001 edition, 04 2017.
- [2] G. Collins and T. C. Johnson. Chapter 37 - Ganymede and Callisto. Elsevier, 2014. URL <https://doi.org/10.1016/B978-0-12-415845-0.00037-2>.
- [3] S. Graf, K. Altweg, H. Balsiger, A. Jäckel, E. Kopp, U. Langer, W. Luithardt, C. Westermann, and P. Wurz. A cometary neutral gas simulator for gas dynamic sensor and mass spectrometer calibration : Space simulations in laboratory: Experiments, instrumentation, and modeling. Journal of Geophysical Research, 109, 2004.
- [4] C. R. G.Wells, H. Prest. Technical Note: Signal, Noise and Detection Limits in Mass Spectrometry. Agilent Technologies. doi: 5990-7651EN.
- [5] A. E. Hedin, C. P. Avery, and C. D. Tschetter. An analysis of spin modulation effects on data obtained with a rocket-borne mass spectrometer. Journal of Geophysical Research, 69(21):4637–4648, nov 1964. doi: 10.1029/jz069i021p04637. URL <https://doi.org/10.1029%2Fjz069i021p04637>.
- [6] L. Hofer. Development of the gas chromatograph – mass spectrometer to investigate volatile species in the lunar soil for the Luna-Resurs mission. Universität Bern, 2015.
- [7] D. Lasi, S. Meyer, D. Piazza, M. Lüthi, A. Nentwig, M. Gruber, S. Brüngger, M. Gerber, S. Braccini, M. Tulej, M. Föhn, and P. Wurz. Decisions and trade-offs in the design of a mass spectrometer for jupiter’s icy moons. In 2020 IEEE Aerospace Conference, pages 1–20, 2020. doi: 10.1109/AERO47225.2020.9172784.
- [8] S. Meyer. Development of Fully Automated and Highly Precise Data Analysis for a Miniaturized Laser-Ablation Mass Spectrometer. Universität Bern, 2013.
- [9] S. Meyer. In situ mass spectrometry for planetary exploration: Quantitative chemical composition measurements on planetary surfaces. Universität Bern, 2015.
- [10] S. Meyer. Development of a Neutral Gas-and Ion-Mass Spectrometer for Jupiter’s Moons. Universität Bern, 2017.
- [11] S. Meyer, M. Tulej, and P. Wurz. Mass spectrometry of planetary exospheres at high relative velocity: direct comparison of open- and closed-source measurements. Geoscientific Instrumentation, Methods and Data Systems, 6(1):1–8, 2017. doi: 10.5194/gi-6-1-2017. URL <https://gi.copernicus.org/articles/6/1/2017/>.
- [12] S. Scherer. Design of a high-performance Reflectron Time-of-Flight mass spectrometer for space applications. Universität Bern, 1999.
- [13] D. van Essen and W. C. Heerens. On the transmission probability for molecular gas flow through a tube. Journal of Vacuum Science and Technology, 13(6):1183 – 1187, 1976.
- [14] M. Wüest, D. S. Evans, and R. von Steiger. Calibration of Particle Instruments in Space Physics. 2007.

- [15] P. Wurz. Lecture notes mass spectrometry and ion optics, 2017.

7 Appendix

Acknowledgement

My thanks go to:

Prof. Dr. Peter Wurz for the opportunity to work on such a versatile experiment. The work was very instructive from the physical and the technical point of view. I also appreciated the educational discussions. Enduring my shenanigans.

Stefan Meyer who introduced me to the work with the ILENA test facility and who had always an open ear for my questions at the beginning of this thesis.

Harald Mischler and the team from the mechanic's workshop of the University of Bern and also to my office colleagues Georg Bodmer, Adrian Etter and Joël Gonseth for their technical support in the laboratory and the amusing discussions in our office.

my friends with whom I had so many distracting and constructive discussions especially during our weekly coffee breaks.

Erklärung

gemäss Art. 28 Abs. 2 RSL 05

Name/Vorname: Föhn Martina

Matrikelnummer: 11-105-145

Studiengang: Master of Science in Physics

Bachelor

Master

Dissertation

Titel der Arbeit: Application of Surface Physics for Instruments in Space Science

LeiterIn der Arbeit: Prof. Dr. Peter Wurz

Ich erkläre hiermit, dass ich diese Arbeit selbständig verfasst und keine anderen als die angegebenen Quellen benutzt habe. Alle Stellen, die wörtlich oder sinngemäss aus Quellen entnommen wurden, habe ich als solche gekennzeichnet. Mir ist bekannt, dass andernfalls der Senat gemäss Artikel 36 Absatz 1 Buchstabe r des Gesetzes vom 5. September 1996 über die Universität zum Entzug des auf Grund dieser Arbeit verliehenen Titels berechtigt ist.
Ich gewähre hiermit Einsicht in diese Arbeit.

Ort/Datum

Unterschrift